Island Arc

Island Arc (2013)

Research Article

Geodynamic evolution of a forearc rift in the southernmost Mariana Arc

Julia M. Ribeiro,[1] Robert J. Stern,[1] Fernando Martinez,[2] Osamu Ishizuka,[3,10] Susan G. Merle,[4] Katherine Kelley,[5] Elizabeth Y. Anthony,[6] Minghua Ren,[6] Yasuhiko Ohara,[7,10] Mark Reagan,[8] Guillaume Girard,[8] and Sherman Bloomer[9]

[1]*Geosciences Department, University of Texas at Dallas, 800 W. Campbell Rd. Richardson, Texas 75083-0688, USA (email: juliaribeiro@utdallas.edu),* [2]*Hawai'i Institute of Geophysics and Planetology, SOEST, University of Hawai'i at Manoa, 680 East-West Rd, POST 602, Honolulu, Hawaii 96822 USA,* [3]*AIST, Central 7, Geological Survey of Japan, 1-1-1 Higashi, Tsukuba, Ibaraki 305-8567, Japan,* [4]*NOAA Vents Program, Oregon State University, 2115 SE Oregon State University Dr., Newport, Oregon 97365, USA,* [5]*Graduate School of Oceanography, University of Rhode Island, Narragansett Bay Campus, Narragansett, Rhode Island 02882, USA,* [6]*University of Texas at El Paso, Department of Geological Sciences, 500 West University Avenue, El Paso, Texas 79968, USA,* [7]*Hydrographic and Oceanographic Department of Japan, 2-5-18 Aomi, Koto-ku, Tokyo 135-0064, Japan,* [8]*Department of Geosciences, University of Iowa, 10 Glendale Court, Iowa City, Iowa 52242, USA,* [9]*Geosciences Department, Oregon State University, 128 Kidder Hall, Corvallis, Oregon 97331, USA, and* [10]*Japan Agency for Marine-Earth Science and Technology, Natsushima 2-15, Yokosuka 237-0061, Japan*

Abstract The southernmost Mariana forearc stretched to accommodate opening of the Mariana Trough backarc basin in late Neogene time, erupting basalts at 3.7–2.7 Ma that are now exposed in the Southeast Mariana Forearc Rift (SEMFR). Today, SEMFR is a broad zone of extension that formed on hydrated, forearc lithosphere and overlies the shallow subducting slab (slab depth ≤ 30–50 km). It comprises NW–SE trending subparallel deeps, 3–16 km wide, that can be traced ≥ ~30 km from the trench almost to the backarc spreading center, the Malaguana-Gadao Ridge (MGR). While forearcs are usually underlain by serpentinized harzburgites too cold to melt, SEMFR crust is mostly composed of Pliocene, low-K basaltic to basaltic andesite lavas that are compositionally similar to arc lavas and backarc basin (BAB) lavas, and thus defines a forearc region that recently witnessed abundant igneous activity in the form of seafloor spreading. SEMFR igneous rocks have low Na_8, Ti_8, and Fe_8, consistent with extensive melting, at ~23 ± 6.6 km depth and 1239 ± 40°C, by adiabatic decompression of depleted asthenospheric mantle metasomatized by slab-derived fluids. Stretching of pre-existing forearc lithosphere allowed BAB-like mantle to flow along the SEMFR and melt, forming new oceanic crust. Melts interacted with pre-existing forearc lithosphere during ascent. The SEMFR is no longer magmatically active and post-magmatic tectonic activity dominates the rift.

Key words: forearc rift, Mariana arc, seafloor spreading, subduction zone.

INTRODUCTION

Forearcs are cold regions above subduction zones that lie between the trench and the magmatic arc. They can be accretionary or non-accretionary depending on the amount of sediment carried into the trench (Lallemand 2001; Stern 2002). Non-accretionary forearcs, such as that of the Marianas, are of special interest as they preserve a record of the first lavas that erupted in association with subduction initiation (Stern & Bloomer 1992; Reagan *et al.* 2010; Ishizuka *et al.* 2011). Forearc lithosphere is underlain by the cold, subducting plate that releases its hydrous fluids into the upper mantle wedge, resulting in exceptionally cold (<400°C; Hulme *et al.* 2010) and serpentinized

Received 31 October 2012; accepted for publication 11 June 2013.

doi:10.1111/iar.12039

mantle lithosphere that rarely melts (Van Keken *et al.* 2002; Hyndman & Peacock 2003; Wada *et al.* 2011). The occurrence of cold, serpentinized forearc mantle beneath the Mariana forearc is demonstrated by eruption of serpentinite mud volcanoes (Mottl *et al.* 2004; Savov *et al.* 2005, 2007; Wheat *et al.* 2008; Hulme *et al.* 2010) and serpentinized peridotite outcrops on the inner trench slope (Bloomer & Hawkins 1983; Ohara & Ishii 1998). Serpentinized mantle beneath the forearc has also been imaged by geophysical surveys (Tibi *et al.* 2008). Ultramafic rocks from the upper mantle wedge found as clasts in mud volcanoes and on the inner trench slope mostly consist of harzburgite, residues of mantle melting (Parkinson & Pearce 1998; Savov *et al.* 2005, 2007) that are chemically distinct from the more fertile, backarc basin (BAB) peridotites (Ohara *et al.* 2002). Such highly depleted, forearc mantle can melt in association with early-arc volcanism to generate boninites (Stern & Bloomer 1992; Reagan *et al.* 2010). Decompression melting of more fertile mantle to form tholeiitic basalts near the trench also has been documented during the first stage of subduction initiation. These lavas have mid ocean ridge basalt (MORB)-like compositions and have been termed forearc basalts (FABs) reflecting their subduction-related origin and location in modern forearcs (Reagan *et al.* 2010).

In the Izu–Bonin–Mariana (IBM) intraoceanic system, most forearc lavas are Eocene–Oligocene in age, and younger forearc lavas are unusual (Stern & Bloomer 1992; Reagan *et al.* 2010; Ishizuka *et al.* 2011). Here, we document the first record of Pliocene forearc lavas from the southernmost Mariana convergent margin, indicating that the mantle can melt beneath forearcs long after subduction initiation. These low-K lavas are tholeiitic basalts generated from BAB-like asthenospheric mantle during seafloor spreading in the Southeast Mariana Forearc Rift (SEMFR), which is a broad zone of deformation (~40 km wide and ~60 km long), extending from the trench to the Fina-Nagu arc Volcanic Chain (FNVC). The SEMFR today overlies a shallow subducting Pacific slab (≤50–100 km deep; Becker 2005).

This paper presents a first report on the geology and tectonic evolution of the SEMFR. We present bathymetry, summarize the results of bottom traverses, and provide petrologic, major element geochemical data, and $^{40}Ar/^{39}Ar$ ages of igneous rocks sampled during two JAMSTEC research cruises. These data are used to characterize SEMFR lavas, to address when, where, and how SEMFR lavas were generated, and to determine sources of the magmas, and conditions of melting. Addressing these issues helps us better understand how such melts were produced in a cold forearc, and allows us to develop a geodynamic model to constrain the geodynamic evolution of the S. Mariana forearc. In this manuscript, we show that SEMFR lavas have BAB-like geochemical and petrographic features, and opening of the Southernmost Mariana Trough allowed adiabatic decompression melting of BAB-like asthenospheric mantle in the forearc to produce SEMFR lavas at 3.7–2.7 Ma.

GEODYNAMIC SETTING

The Mariana intraoceanic arc system is the southern third of the IBM convergent margin. It is generally associated with a sediment-starved forearc ~200 km wide (Fryer *et al.* 2003; Kato *et al.* 2003), submarine and subaerial volcanoes of the active magmatic arc (Baker *et al.* 2008), and a BAB with a spreading axis that generally lies ~250–300 km from the trench (Stern *et al.* 2003). Mariana geodynamic evolution was influenced by collisions with buoyant oceanic plateaus (Ogasawara Plateau in the north and Caroline Ridge in the south). These resisted subduction, stimulating backarc extension to open the Mariana Trough between the collisions (Wallace *et al.* 2005).

The IBM mostly trends N–S but the southernmost Mariana convergent margin (13°10'N–11°N) bends to E–W (Fig. 1a; Bird 2003). This region is deforming rapidly (Martinez *et al.* 2000; Kato *et al.* 2003), accompanied by abundant igneous activity. Here, the Mariana Trench reaches the deepest point on Earth at the Challenger Deep (10994 m; Gardner & Armstrong 2011), and the Pacific–Philippine Sea plate convergence is approximately orthogonal to the trench (Fig. 1a,b; Bird 2003). The tectonic evolution of the southernmost Mariana arc began with the Late Miocene collision of the Caroline Ridge, which pinned the Yap arc and allowed the southern Mariana Trough to open, sculpting the southern termination of the arc (Miller *et al.* 2006b). The southernmost Mariana magmatic arc is poorly developed and entirely submarine, contrasting with the large, often subaerial, arc volcanoes to the north. The arc magmatic front almost intersects the southern end of the BAB spreading center south of 13°N (Fig. 1b; Fryer *et al.* 2003). These features are about 100–150 km from the trench, whereas to the north the BAB

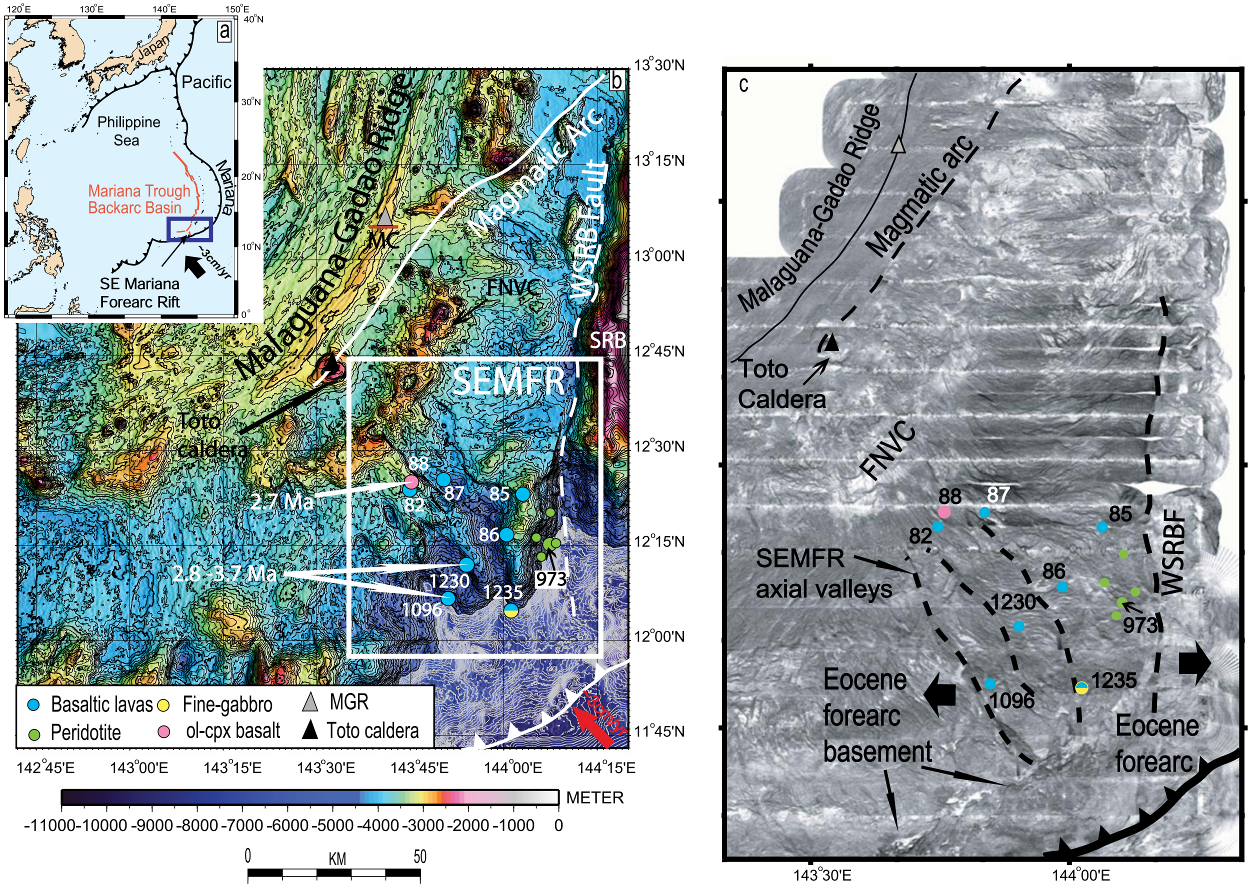

Fig. 1 Locality maps. (a) Izu–Bonin–Mariana (IBM) intraoceanic arc system. The IBM magmatic arc generally lies ~200 km from the trench and the Mariana Trough backarc basin spreading center generally lies ~300 km from the trench. The arrows represent Pacific–Mariana convergence vectors from Kato *et al.* (2003). Blue box shows the area of (b). (b) Bathymetric map of the southernmost Mariana arc-backarc basin system. Southward, the magmatic arc (white line) approaches the Malaguana–Gadao spreading ridge (MGR), both of which lie unusually close (~110 km) to the trench. Location of the Malaguana–Gadao spreading ridge is from Martinez *et al.* (2000). Filled colored circles show locations of YK06-12, YK08-08 Leg 2 and YK10-12 Shinkai dives and YK08-08 Leg 2 YKDT deep-tow cameras; the small circles show the locations of dredge site D27 (Bloomer & Hawkins 1983), Shinkai 6500 dives158 and 159 (Fryer 1993), and dredge sites KH98-1D1 and KH98-1D2 (Sato & Ishii 2011); triangles show the locations of KR00-03 Leg 2 Kaiko dives in Toto caldera and Malaguana–Gadao Ridge. Note that Kaiko dive 164 is near the magma chamber (MC) identified by Becker *et al.* (2010) as shown by the red line. The white box shows the approximate region encompassed by SEMFR. The dashed white line shows the position of the W. Santa Rosa Bank (WSRB) Fault which separates older rocks of the Santa Rosa Bank (SRB) from the SEMFR younger rocks. The white numbers are ^{40}Ar–^{39}Ar radiometric ages. Map generated with GMT (Smith & Wessel 1990; Wessel & Smith 1995b; Wessel & Smith 1998; Wessel & Smith 1995a) by using a compilation from the University of New Hampshire/Center for Coastal and Ocean Mapping/Joint Hydrographic Center (Gardner 2006; Gardner 2007; Gardner 2010). (c) Sidescan sonar (HMR1) image of the S. Mariana convergent margin (Fryer *et al.* 2003) with the location of traverses by JAMSTEC submersibles during YK06-12, YK08-08 Leg 2, YK10-12 and KR00-03 Leg 2 cruises. Dark areas have high backscatter, whitish areas corresponds to low backscatter. The SEMFR, the Malaguana-Gadao Ridge and the Toto caldera are dominated by high backscatter, indicating that the oceanic crust or lightly sedimented basement is exposed. Black short dashed line denotes SEMFR axial deeps, ridges lie between the valleys. Black thick arrows show the opening of SEMFR (Martinez & Stern 2009). FNVC (Fina–Nagu Volcanic Chain) represents extinct arc volcanoes.

spreading axis lies ~250–300 km from the trench and is separated from the magmatic arc by 50–100 km (Fryer *et al.* 1998; Stern *et al.* 2003). The magmatic arc appears to have been reorganized recently, as evidenced by a complex bathymetric high with multiple nested calderas – an inferred paleo-arc (the Fina-Nagu Volcanic Chain in Fig. 1b) where no hydrothermal activity was observed (Baker *et al.* 2008) and calderas are covered with sediments (Fig. 1c) – SE of and parallel to the modern magmatic arc (e.g. Toto caldera). The southern Mariana Trough has a well-defined spreading ridge, the Malaguana-Gadao Ridge (MGR), with a well-developed magma chamber and several hydrothermal vents (Baker *et al.* 2008; Kakegawa *et al.* 2008; Becker *et al.* 2010). Because the subducted Pacific plate lies ~100 km beneath it, the MGR melt source region captures hydrous fluids usually released beneath arc volcanoes, enhancing mantle melting and resulting in an inflated ridge morphology that is unusually robust for the Mariana Trough backarc basin, in spite of anintermediate spreading rate (<65 mm/yr; Fryer *et al.* 1998; Martinez *et al.* 2000; Becker *et al.* 2010). More rapid extension along the MGR might also enhance decompression melting (Becker *et al.* 2010).

The southernmost Mariana convergent margin is underthrust by a narrow slab of Pacific plate (traceable to ~250 km depth; Gvirtzman & Stern 2004), torn N–S at ~144°15'E (Fryer *et al.* 1998; Gvirtzman & Stern 2004). Analogue experiments show that short, narrow subducted slabs trigger toroidal (around the slab edge) and poloidal (underneath the slab tip) asthenospheric mantle flows that generate rapid slab rollback and trench retreat relative to the upper plate (Funiciello *et al.* 2003, 2006; Schellart *et al.* 2007). These conditions lead to weak coupling of the subducting plate with the overriding plate, stimulating rapid deformation of the overriding plate (i.e., the southern Mariana Trough) and may be responsible for the very narrow forearc that defines the southern Mariana margin west of the W. Santa Rosa Bank Fault (Fig. 1b, Gvirtzman & Stern 2004). The unusual tectonic situation of the southernmost Mariana convergent margin has also affected magmagenesis. Sub-forearc mantle usually is too cold to melt (Van Keken *et al.* 2002; Wada *et al.* 2011), so that slab-derived fluids only lead to serpentinization (Hyndman & Peacock 2003). Instead, the dynamic tectonic setting of the southern Marianas results in mantle melting much closer to the trench than is normally observed.

GEOLOGY AND MORPHOLOGY OF THE SOUTHEAST MARIANA FOREARC RIFT

Most of the IBM convergent margin is underlain by lithosphere that formed after subduction began ~52 Ma (Reagan *et al.* 2010; Ishizuka *et al.* 2011). In the southernmost Marianas, Eocene forearc lithosphere was stretched in late Neogene time to accommodate the opening of the Mariana Trough BAB; part of this extension is localized along the SEMFR (Martinez & Stern 2009). The morphological expression of the SEMFR is apparent over a region ~40 km wide and at least 60 km long (Supporting Information Table S1.2). The SEMFR is composed of broad southeast-trending deeps and ridges (Fig. 1b), each 50 to 60 km long and 3 to 16 km wide, which opened nearly parallel to the trench axis. These rifts can be traced from the Mariana Trench almost to the FNVC (Fig. S1.1 in Supporting Information S1). Eastward, the SEMFR is bounded by a N–S fault, the W. Santa Rosa Bank Fault (WSRBF, Fig. 1b; Fryer *et al.* 2003), which separates thick crust of the broad Eocene forearc to the north and east (including that beneath Santa Rosa Bank) from the deeper and narrower forearc of the S. Marianas – including the SEMFR – to the west. The WSRBF also appears to overlie a tear in the subducted slab (Fryer *et al.* 2003; Gvirtzman & Stern 2004). The WSRBF is taken to be the eastern boundary of the SEMFR because it does not have the same NNE–SSW trend as the three SEMFR deeps (Fig. 1b), and the forearc is significantly older to the east (Reagan *et al.* 2010). The SEMFR overlies the shallow part of the slab (≤30–100 km deep, Becker 2005) and is situated in a region with numerous shallow (crustal) earthquakes, (Martinez & Stern 2009) signifying active deformation.

We studied the SEMFR by interpreting swath-mapped bathymetry and previously published HMR-1 sonar backscatter imagery (Martinez *et al.* 2000). The region is characterized by high sonar backscatter, indicating little sedimentary cover (Fig. 1c). This was confirmed by Shinkai 6500 manned submersible and YKDT deep-tow camera/dredge seafloor studies. Table S1.1 in Supporting Information S1 summarizes the position and lithologies encountered during these dives (Fig. 1b). Most dives recovered basalt. In addition, deeper crustal and upper mantle lithologies, e.g. diabase, fine-grained gabbros and deformed peridotites, were recovered near the WSRBF (Supporting Information Figs S1.7 and

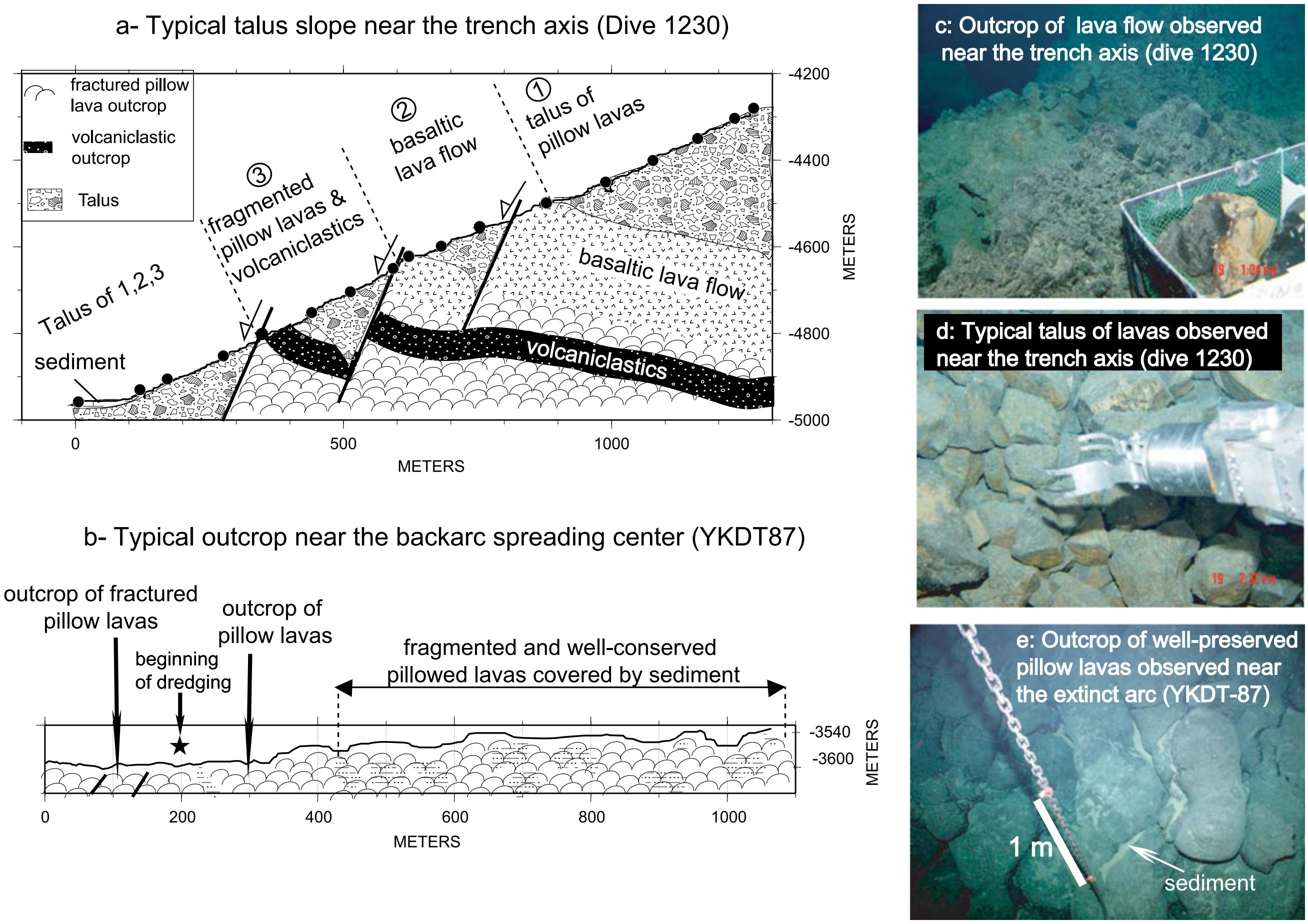

Fig. 2 Typical bottom profiles of SEMFR encountered during seafloor traverses. (a) near the trench axis (Shinkai 6500 dive 1230) and (b) near the Fina–Nagu Volcanic Chain (FNVC; YKDT-87). Near the trench, SEMFR flanks are dominated by steep talus slopes of lava fragments with few exposures of tilted and faulted lava flows. Talus and outcrops are covered by thin pelagic sediment. Near the FNVC, SEMFR relief is smoother with better-preserved pillow lava outcrops covered by thin sediment. Photographs of the typical seafloor observed near the trench (c, d) and near the FNVC (e). Black star in (b) shows the beginning of YKDT deep-tow camera dredging.

S1.8). Similar lithologies are also reported by previous studies of the area (Bloomer & Hawkins 1983, Fryer, 1993, Michibayashi *et al.* 2009; Sato & Ishii 2011). Based on relief, the SEMFR can be subdivided along strike into NW, central, and SE sectors. The SEMFR relief is most rugged in the SE sector near the trench, where it is intensely faulted and affected by landsliding, with abundant talus slopes of fragmented basaltic lavas (Fig. 2a,c,d and Figs S1.5 to S1.8 in Supporting Information). The central SEMFR is less faulted, with more outcrops and less talus, but still has many steep talus slopes and faulted lava flows (Figs S1.9-S1.10 in Supporting Information). The NW SEMFR, nearest the MGR, has gentler relief, with better-preserved pillow lava outcrops (Fig. 2b,e and Figs S1.11–S1.13 in Supporting Information). We did not recover samples of Paleogene forearc crust in the SEMFR, although this is common to the NE and west, indicating that SEMFR is floored by young, tectonized oceanic crust. Our bottom observations along with the absence of parallel magnetic fabrics in the SEMFR (Martinez *et al.* 2000) suggest that the SEMFR is no longer a site of active volcanism.

Toto caldera and part of the MGR near the NW limit of the SEMFR were studied during ROV Kaiko Dives 163 and 164 (R/V Kairei cruise KR00-03 Leg 2, Fig. 1b). Toto caldera, which may be part of the immature magmatic arc, is mostly covered by talus of fresh lava fragments with a whitish coating, perhaps bacteria or sulfur-rich precipitate (Supporting Information Fig. S1.14), derived from the active Nakayama hydrothermal site (Gamo *et al.* 2004; Kakegawa *et al.* 2008). The MGR seafloor is mostly composed of fresh, well-preserved pillow lavas alternating with aa and solidified lava lake (Becker *et al.* 2010), along with active hydrothermal vents (Supporting Information Fig. S1.15) indicating ongoing magmatic activity. Figure 1c shows high sonar backscatter for Toto caldera and around the MGR, indicating hard rock (fresh lava) exposures and thin sediments, consistent with seafloor seen in dive videos.

METHODS

Igneous rock samples were collected during two cruises YK08-08 Leg 2 (Shinkai 6500 manned submersible dive 1096) in 2008 and YK10-12 (Shinkai 6500 dives 1230, 1235 and Yokosuka deep-tow camera dredge (YKDT) 85, 86, and 88) in 2010. Representative, fresh samples were selected onboard for petrographic and geochemical studies. Information from Kaiko ROV dives 163 and 164(R/V Kairei cruise KR00-03 Leg 2 in 2000) is also included. High-resolution videos of the seafloor generated during dives were reviewed during and after the cruises (see Supporting Information S1 for more details). GMT (Smith & Wessel 1990; Wessel & Smith 1995a,b, 1998) was used to compile SEMFR bathymetric data, including swathmapping results from these cruises and those of Gardner (2006), Gardner (2007), and Gardner (2010). Maps were imported into ArcGIS to generate bathymetric cross sections perpendicular to the strike of the SEMFR (Fig. S1.1 in Supporting Information).

Igneous rock samples were analyzed, using the procedures reported in Supporting Information S2. For major element analyses, fresh sample chips containing as few phenocrysts as possible were hand-picked and powdered in an alumina ball mill. Whole rock chemical analyses for Shinkai dive 1096 samples were carried out on Philips PW1404 X-ray fluorescence (XRF) spectrometer at the Geological Survey of Japan/AIST. External errors and accuracy are < 2%. Whole rock chemical analyses for other samples were performed at the University of Rhode Island by fusion–dissolution of glass beads; and analyses were conducted using an Ultima-C Jobin Yvon Horiba Inductively Coupled Plasma Atomic Emission Spectroscopy (ICP–AES) at Boston University. Glass beads were generated by melting 400 ± 5 mg of lithium metaborate ($LiBO_4$) flux with 100 ± 5 mg of ignited sample powder at 1050°C for 10 min. Molten beads were dissolved in 5% nitric acid to achieve a final dilution factor of ~4000 (Kelley *et al.* 2003). Calibration curves for ICP–AES data yield $r^2 \geq 0.999$, reproducibility of replicate analyses are ≤ 3% rsd for each element, and major element oxides sum to 99 ± 1 wt%. Replicates of samples analyzed by ICP–AES and XRF yield averaged reproducibility < 4% rsd for each element. Results are reported in Table 1.

For mineralogical chemistry analyses, polished thin sections were prepared for 16 samples. These were analyzed using the Cameca SX-50 electron microprobe at University of Texas at El Paso. Multiple point analyses give a mean value with 1σ precision ≤ 1 wt% for each selected mineral.

Four samples were dated by step-heating ^{40}Ar–^{39}Ar at the Geological Survey of Japan/AIST on a VG Isotech VG3600 noble gas mass spectrometer fitted with a BALZERS electron multiplier. Further details of procedures are reported in Supporting Information S2.

RESULTS

ROCK DESCRIPTION

Here we outline the principal petrographic and mineralogical features of igneous rocks sampled from the SEMFR, Toto caldera, and MGR. The method for sample description is reported in Supporting Information S3 and detailed sample descriptions are provided in Supporting Information S4. The SEMFR lavas are mostly aphyric (<1% phenocrysts) and sparsely phyric (1–5% phenocrysts) basalts and basaltic andesites, indicating eruption at near-liquidus temperatures. These are microporphyritic pillows or massive flows, with thin, microcrystallite-rich glassy rims (1–11 mm of fresh, translucent to dark brown glass), thin (≤1 mm) Mn coat, and negligible alteration (Fig. 3). Pillow lavas are vesicular despite being collected at ~6000–3000 m, indicating that these magmas contained significant volatiles. In contrast, basaltic massive lava flows are more crystalline and less vesicular. Embayed phenocrysts indicate disequilibrium, perhaps due to magma mixing. Pillowed lavas sampled in the NW (YKDT-88) contain larger crystals (≥0.5 mm) of clinopyroxene and olivine set in a finely microcrystalline olivine-rich groundmass (Fig. 3c). Similar olivine-rich lavas were not sampled elsewhere in the SEMFR. Diabase and fine-grained gabbros were also recovered near the WSRB fault (Shinkai

Table 1 Major (wt%) element compositions of SE Mariana Forearc Rift (SEMFR) lavas

Sample No. / IGSN	1096-R2* SEMFR JMR000011	1096-R3 SEMFR JMR000012	1096-R4 SEMFR JMR000013	1096-R7 SEMFR JMR000016	1096-R8 SEMFR JMR000017	1096-R11 SEMFR JMR00001A	1096-R12 SEMFR JMR00001B	1096-R15 SEMFR JMR00001D	1096-R16 SEMFR JMR00001E	1096-R17 SEMFR JMR00001F	1096-R19 SEMFR JMR00001H	1096-R20 SEMFR JMR00001I	1096-R21 SEMFR JMR00001J
Method	–	XRF	XRF	XRF	XRF	XRF	XRF	XRF	XRF	XRF	XRF	XRF	XRF
Sample description	Pillow	pillow	pillow	pillow	pillow	pillow	Pillow	pillowed	Pillowed	pillowed	pillowed	pillowed	pillowed
	Lava	basalt	basalt	basalt	basalt	basalt	basalt	ol basalt	ol basalt	ol basalt	ol basalt	ol basalt	ol basalt
SiO2	–	52.50	52.73	52.60	52.58	52.57	52.45	50.56	50.52	50.69	50.04	50.77	50.64
TiO2	–	0.97	0.98	0.97	0.96	1.01	0.96	0.69	0.67	0.66	0.65	0.69	0.67
Al2O3	–	16.34	16.64	16.55	16.36	16.31	16.60	16.28	15.94	16.29	16.12	16.35	16.01
FeO	–	8.73	8.38	8.44	8.64	8.75	8.65	7.47	7.47	7.25	7.29	7.19	7.51
MnO	–	0.16	0.14	0.15	0.15	0.15	0.15	0.13	0.13	0.13	0.13	0.12	0.13
MgO	–	5.00	4.78	4.74	4.95	4.92	4.88	7.35	8.08	7.79	8.14	7.19	8.00
CaO	–	9.60	9.69	9.71	9.56	9.36	9.76	12.81	13.09	13.36	13.45	13.06	12.95
Na2O	–	3.31	3.33	3.30	3.28	3.30	3.33	2.27	2.14	2.14	2.14	2.29	2.18
K2O	–	0.53	0.56	0.57	0.55	0.57	0.52	0.36	0.25	0.27	0.20	0.23	0.26
P2O5	–	0.11	0.11	0.11	0.11	0.12	0.11	0.08	0.07	0.07	0.07	0.08	0.07
total	–	98.22	98.27	98.06	98.09	98.04	98.37	98.82	99.20	99.46	99.03	98.77	99.26
%LOI													
Mg#	–	50.52	50.42	50.05	50.56	50.04	50.14	63.68	65.85	65.70	66.55	64.06	65.50
Na8								2.09	2.16	2.09	2.16	2.05	2.20
Ti8								0.62	0.67	0.64	0.66	0.60	0.67
Fe8								6.62	7.53	7.00	7.37	6.09	7.56
40Ar-39Ar ages (Ma)	3.5 ± 0.4								3.7 ± 0.3				
T(°C)								1246	1245	1236	1240	1235	1246
P(GPa)								0.77	0.73	0.69	0.73	0.68	0.74

Sample No. / IGSN	1096-R22 SEMFR JMR00001K	1096-R23 SEMFR JMR00001L	1096-R28 SEMFR JMR00001N	1096-R8 SEMFR JMR000017	1096-R21 SEMFR JMR00001J	1230-R2 SEMFR JMR00001O	1230-R8 SEMFR JMR00001T	1230-R10 SEMFR JMR00001U	1230-R11 SEMFR JMR00001V	1230-R14 SEMFR JMR00001W	1230-R21 SEMFR JMR000020	1230-R22 SEMFR JMR000021	1230-R25 SEMFR JMR000023
Method	XRF	XRF	XRF	ICP–AES	ICP–AES	ICP–AES	ICP–AES	ICP–AES	ICP–AES	ICP–AES	ICP–AES	ICP–AES	ICP–AES
Sample description	pillowed	pillowed	pillowed	pillow	pillowed	pillowed	vesicular	subaphyric	aphyric	aphyric	basaltic	basaltic	pillowed
	ol basalt	ol basalt	ol basalt	basalt	ol basalt	ol basalt	basalt	basalt	basalt	basalt	lava flow	lava flow	pl basalt
SiO2	50.74	50.74	50.62	53.57	51.26	51.53	52.78	52.55	52.65	52.81	51.56	54.13	51.93
TiO2	0.67	0.74	0.65	0.94	0.65	0.85	1.40	1.12	0.99	0.94	0.86	1.03	1.04
Al2O3	16.20	16.35	15.86	16.84	16.57	17.06	16.53	16.74	17.31	17.32	17.08	16.88	17.11
FeO	7.43	8.10	7.40	8.67	7.16	8.01	9.92	8.92	8.71	7.96	7.55	8.10	8.17
MnO	0.12	0.16	0.13	0.15	0.13	0.14	0.14	0.12	0.15	0.14	0.10	0.12	0.14
MgO	7.21	7.23	8.36	5.06	8.08	6.34	3.87	5.46	5.73	6.00	6.27	5.28	5.82
CaO	13.24	12.43	13.04	9.30	12.96	11.21	8.83	9.86	10.12	11.23	11.74	9.86	10.84
Na2O	2.19	2.33	2.12	3.07	2.17	2.56	3.79	3.02	3.12	2.92	3.06	3.33	3.20

Table 1 *Continued*

Sample No. / IGSN	1096-R22 SEMFR JMR00001K	1096-R23 SEMFR JMR00001L	1096-R28 SEMFR JMR00001N	1096-R8 SEMFR JMR000017	1096-R21 SEMFR JMR00001J	1230-R2 SEMFR JMR00001O	1230-R8 SEMFR JMR00001T	1230-R10 SEMFR JMR00001U	1230-R11 SEMFR JMR00001V	1230-R14 SEMFR JMR00001W	1230-R21 SEMFR JMR000020	1230-R22 SEMFR JMR000021	1230-R25 SEMFR JMR000023
Method	XRF	XRF	XRF	ICP–AES	ICP–AES	ICP–AES	ICP–AES	ICP–AES	ICP–AES	ICP–AES	ICP–AES	ICP–AES	ICP–AES
Sample description	pillowed	pillowed	pillowed	pillow	pillowed	pillowed	vesicular	subaphyric	aphyric	aphyric	basaltic	basaltic	pillowed
	ol basalt	ol basalt	ol basalt	basalt	ol basalt	ol basalt	basalt	basalt	basalt	basalt	lava flow	lava flow	pl basalt
K2O	0.23	0.28	0.32	0.53	0.26	0.40	0.97	0.25	0.44	0.41	0.42	0.37	0.47
P2O5	0.07	0.08	0.07	0.12	0.07	0.09	0.18	0.13	0.12	0.11	0.11	0.12	0.13
total	98.92	99.33	99.38	98.26	99.31	98.21	98.42	98.18	99.34	99.84	98.74	99.20	98.84
%LOI				0.96%	0.59%	0.93%	1.89%	1.11%	1.24%	1.09%	1.35%	1.06%	1.09%
Mg#	63.37	61.43	66.83	51.02	66.82	58.56	41.02	52.22	54.00	57.35	59.71	53.80	55.95
Na8	1.95	2.08	2.13		2.19								
Ti8	0.58	0.63	0.65		0.66								
Fe8	6.32	6.95	7.44		7.21								
40Ar-39Ar ages (Ma)						2.8 ± 0.5							
T(°C)	1245	1269	1241										
P(GPa)	0.71	0.87	0.72										

Sample No. / IGSN	1230-R26 SEMFR JMR000024	1230-R33 SEMFR JMR000027	1235-R2 SEMFR JMR000029	1235-R8 SEMFR JMR00002C	1235-R11 SEMFR JMR00002E	1235-R12 SEMFR JMR00002F	1235-R13 SEMFR JMR00002G	1235-R17 SEMFR JMR00002I	1235-R20 SEMFR JMR00002L	85-R6 SEMFR JMR00002R	85-R11 SEMFR JMR00002T	85-R12 SEMFR JMR00002U	86-R7 SEMFR JMR00002X
Method	ICP–AES	ICP–AES	ICP–AES	ICP–AES	ICP–AES	ICP–AES	ICP–AES	ICP–AES	ICP–AES	ICP–AES	ICP–AES	ICP–AES	ICP–AES
Sample description	Pillowed	pillowed	aphyric	fg basalt	diabase	fg ol basalt	fg gabbro	fg gabbro	fg gabbro	pillowed	pillowed	pillowed	cobble /
	pl basalt	pl basalt	Basalt							pl basalt	pl basalt	pl basalt	pl basalt
SiO2	51.16	51.53	56.14	52.98	50.61	49.94	52.28	49.49	52.60	51.46	50.83	52.19	50.41
TiO2	1.02	1.07	1.35	0.77	0.74	0.78	1.02	0.80	0.91	1.06	0.99	1.06	0.83
Al2O3	17.12	17.22	15.15	16.53	17.40	17.48	17.19	16.92	16.42	16.68	16.87	16.27	18.38
FeO	8.26	7.99	9.93	7.75	6.76	7.74	7.61	7.83	8.76	8.68	8.03	8.79	6.77
MnO	0.15	0.13	0.16	0.13	0.13	0.17	0.14	0.14	0.15	0.15	0.14	0.15	0.13
MgO	6.44	5.61	4.30	6.77	8.91	6.80	6.52	7.89	5.96	6.17	6.43	6.62	7.44
CaO	10.99	10.92	4.56	9.80	11.03	12.48	10.55	11.15	9.49	11.02	11.86	11.48	12.75
Na2O	2.89	3.08	6.62	3.81	3.64	2.85	3.69	3.80	3.64	2.79	2.79	2.86	2.69
K2O	0.41	0.44	0.09	0.17	0.13	0.27	0.21	0.09	0.40	0.41	0.35	0.29	0.16
P2O5	0.13	0.13	0.18	0.09	0.09	0.11	0.13	0.08	0.13	0.12	0.11	0.12	0.10
total	98.57	98.13	98.49	98.80	99.43	98.63	99.34	98.19	98.46	98.56	98.40	99.85	99.66
%LOI	1.03%	1.86%	1.60%	2.54%	4.21%	0.52%	2.03%	4.02%	2.42%	1.26%	1.05%	1.05%	0.49%
Mg#	58.19	55.64	43.61	60.93	70.18	61.08	60.46	64.27	54.85	55.95	58.82	57.36	66.25
Na8													2.50
Ti8													0.74
Fe8													5.90
40Ar-39Ar ages (Ma)													
T(°C)													1219
P(GPa)													0.77

Table 1 *Continued*

Sample No. / IGSN	86-R20 SEMFR JMR00002Z	86-R21 SEMFR JMR000030	88-R1 SEMFR JMR000032	88-R2 SEMFR JMR000033	**MEAN SEMFR**	**STD. DEV.**	163-1-3R Toto caldera JMR000038	163-3-4R Toto caldera JMR00003B	164-1R MGR JMR000034	164-3R MGR JMR000036	164-4R MGR JMR000037
Method	ICP–AES	ICP–AES	ICP–AES	ICP–AES			ICP–AES	ICP–AES	ICP–AES	ICP–AES	ICP–AES
Sample description	cobble /	cobble /	pillowed	pillowed			pillow	pillow	pillow	pillow	pillow
	pl basalt	pl basalt	ol-cpx basalt	ol-cpx basalt			lava	lava	lava	lava	lava
SiO2	51.84	52.77	50.21	50.58	**51.73**	**1.30**	54.23	54.02	60.68	57.92	57.19
TiO2	0.86	1.09	0.36	0.36	**0.88**	**0.22**	0.96	0.97	1.14	1.31	1.30
Al2O3	17.32	16.92	16.16	15.92	**16.66**	**0.57**	16.16	16.60	15.42	15.84	16.13
FeO	7.81	9.24	6.96	6.81	**8.04**	**0.78**	8.78	8.62	7.97	9.12	8.90
MnO	0.14	0.16	0.13	0.13	**0.14**	**0.01**	0.14	0.15	0.17	0.17	0.17
MgO	6.55	5.17	9.90	10.17	**6.53**	**1.46**	5.39	5.42	2.17	3.27	3.20
CaO	11.62	9.86	14.19	14.22	**11.17**	**1.84**	9.58	9.49	5.48	6.77	6.72
Na2O	2.74	3.22	1.17	1.10	**2.93**	**0.87**	2.83	2.50	4.64	3.99	3.99
K2O	0.44	0.67	0.13	0.15	**0.36**	**0.18**	0.27	0.40	0.41	0.34	0.33
P2O5	0.10	0.14	0.03	0.03	**0.10**	**0.03**	0.12	0.13	0.28	0.24	0.23
total	99.41	99.23	99.24	99.46	**98.84**	**0.54**	98.46	98.30	98.36	98.97	98.18
%LOI	0.56%	1.42%	0.59%	0.51%	**1.42%**	**0.95%**	0.09%	0.81%	1.66%	1.72%	1.69%
Mg#	59.94	49.95	71.74	72.73	**58.50**	**7.42**	52.27	52.92	32.68	38.98	39.10
Na8			1.18	1.10	**1.99**	**0.40**					
Ti8			0.36	0.36	**0.60**	**0.11**					
Fe8			7.01	6.84	**6.91**	**0.54**					
40Ar-39Ar ages (Ma)				2.7 ± 0.3							
T(°C)			1225	1217	**1238.76**	**14.01**					
P(GPa)			0.51	0.45	**0.70**	**0.11**					

Mg# [=atomic (Mg^{2+} * 100)/(Mg^{2+} + Fe^{2+})] was calculated assuming all the iron is Fe^{2+} on anhydrous basis. Primitive samples with 7 wt% ≤ MgO < 8 wt% were corrected on anhydrous basis by using the equations of Klein and Langmuir (1987) for Na_8 and Fe_8, and Taylor and Martinez (2003) for Ti_8. See text for details. Sample numbers with * have no major element data reported; minor element data will be reported elsewhere. Fg, fine-grained; ol, olivine; pl, plagioclase; cpx, clinopyroxene

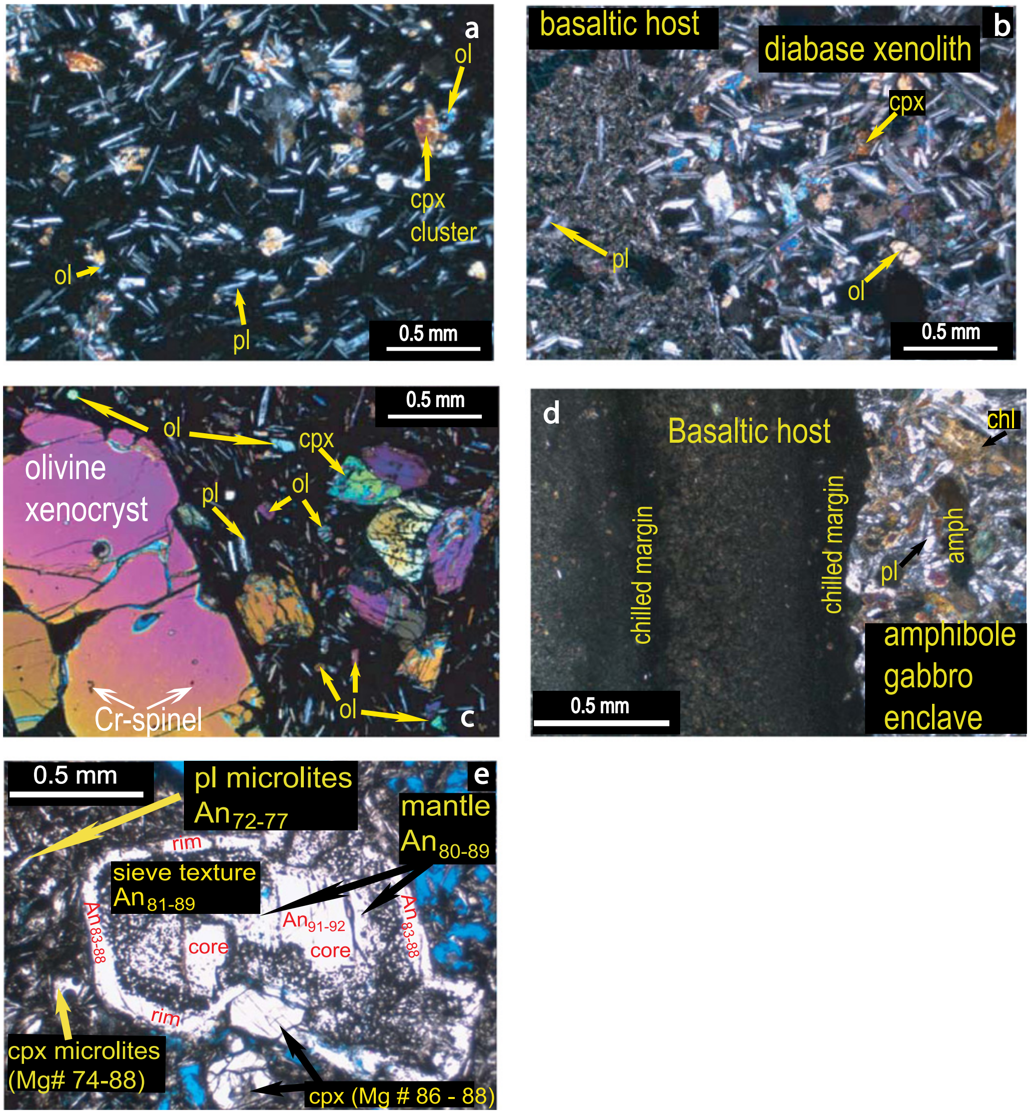

Fig. 3 Photomicrographs of SEMFR lavas and fine gabbro. (a) Typical microporphyritic olivine – clinopyroxene basalt (sample 1230-R2) with microlitic groundmass and microphenocrysts of plagioclase (pl) and clinopyroxene (cpx). (b) Fine-grained diabase xenolith (sample 1235-R12) hosted by microcrystalline basalt (finer grained part to left). The diabase contains Mg-rich olivine (Fo_{89}), Mg-rich clinopyroxene (Mg# $\geq$ 80) and normally zoned Ca-rich plagioclase ($\geq$0.1 mm). In contrast, the basaltic host is more fractionated, with Fe-rich olivine (Fo_{85-86}) and Mg-rich clinopyroxene microphenocrysts ($\geq$0.1 mm). Clinopyroxene in the groundmass (< 0.1 mm) are Mg-poor and coexist with Ca-poor plagioclase microlites. Clinopyroxenes in the diabase exhibit oscillatory and reverse zoning. The boundary between the two textural realms is straight, suggesting that basalt magma picked up solidified diabase. See Supporting Information S4 for more details. (c) Olivine–clinopyroxene basalt from YKDT-88 containing large olivine xenocrysts surrounded by olivine-rich groundmass. (d) Photomicrograph of cryptocrystalline plagioclase basalt from Shinkai dive 1235 (sample 1235-R8) hosting an amphibole gabbro xenolith (chl, chlorite; amph, amphibole). The contact between gabbro and basalt is an irregular chilled margin, suggesting that the basalt picked up solid pieces of gabbro. A second chilled margin is observed inside the basalt, suggesting multiple magmatic injections in the basalt. (e) Photomicrograph of plagioclase (pl) xenocryst observed in the Shinkai dive 1230 (sample 1230-R17). The core of the plagioclase is well-preserved and exhibits An_{91-92} content. The mantle exhibits An_{80-89} and is mostly resorbed (sieve-texture) due to the interaction plagioclase-melt. The rim is well-preserved and is An_{83-88}. Plagioclase microlites have lower An content (An < 80%). Larger, Mg-rich clinopyroxenes (cpx) occur near the An-rich plagioclase xenocrysts (Mg# = 86–88), while the clinopyroxenes microlites exhibit higher range in Mg# (74–88). Such An-rich plagioclases are observed in the arc crust. See Supporting Information S4 for details.

6500 dive 1235; Fig. 3b,d). These might represent the lower crust of the SEMFR (dike complex and gabbro layer).

Pillow lavas from the MGR are very fresh, with translucent glassy rinds. Lavas are vesicular, cryptocrystalline andesites with a glassy groundmass and <1% plagioclase microlites. Lava flows from the Toto caldera are vesicular, sparsely phyric to aphyric, fine-grained to cryptocrystalline basaltic andesites.

MAJOR ELEMENT AND MINERAL COMPOSITIONS

The SEMFR lavas are fresh basalts and basaltic andesites, with 50.4 to 57.0 wt% SiO_2 (data reported are adjusted to 100% total on an anhydrous basis, Fig. 4a). In terms of normative compositions, all lavas are quartz tholeiites. These define a low-K to medium-K suite, with $K_2O < 1$ wt%. Lava compositions cluster along the tholeiitic–calc-alkaline boundary on a plot of FeO*/MgO vs. SiO_2 (Fig. 4b; Miyashiro 1974), or along the medium-Fe/low-Fe boundary (Arculus 2003). Lavas recovered during Shinkai 6500 dive 1096 and 1230 and YKDT-86 and –88 are relatively primitive, with whole rock Mg# (= atomic Mg * 100/(Mg + Fe)) > 60, Fig. 4c). Other SEMFR samples are significantly more fractionated, with Mg# = 41–60. Composition of SEMFR lavas is reported in Table 1. The MGR and Toto caldera lavas are mostly andesites (SiO_2 = 55.1–61.7 wt%, with $K_2O < 0.5$ wt% and Mg# = 33–53). None of the studied lavas are boninitic (MgO > 8 wt%, $SiO_2 > 52$ wt%, $TiO_2 < 0.5$ wt%; Le Bas 2000). Toto caldera lavas plot within the compositional field of southernmost Mariana volcanic arc lavas (SMA: 13°10'N–11°N, Kakegawa *et al.* 2008; Stern *et al.* 2013), suggesting that the Toto caldera belongs to the S. Mariana arc volcanoes (SMA). Toto caldera samples also cluster along the tholeiitic–calc-alkaline boundary. In contrast, MGR lavas are tholeiitic (medium-Fe to high-Fe) basaltic andesites and andesites (Kakegawa *et al.* 2008; Pearce *et al.* 2005; Fig. 4a,b). The Fe enrichment of the MGR lavas (Fig. 4b) suggests that their parental magmas contain less water, inhibiting early crystallization of Fe-oxides. In Figure 4a, MGR lavas do not plot along the SEMFR fractionation trend, and their similar K_2O content suggests that MGR and SEMFR lavas interacted with similar arc-like slab-derived fluids. FABs (Reagan *et al.* 2010) are low-K to medium-K basalt to basaltic andesites that plot within the tholeiitic and calc-alkaline fields (Fig. 4b,c); and the SEMFR plots along the FAB fractional trend (Fig. 4c,d). All lavas from the southernmost Marianas suggest fractionation controlled by plagioclase, clinopyroxene ± olivine crystallization trend (Fig. 4c,f).

The SEMFR basalts and basaltic andesites contain olivine, clinopyroxene, and plagioclase. Results for representative mineral composition are listed in Supporting Information Tables S4.1 to S4.4 and summarized in Table 2. Mineral compositions correlate with whole rock chemical compositions (Fig. 5a,b and Supporting Information S5). Near-primitive (Mg# > 60), olivine-rich SEMFR lavas (Shinkai dive 1096, upper series and YKDT-88) contain Mg-rich olivines ($Fo_{86–88}$) in equilibrium with Mg-rich clinopyroxene (Mg# = 83–91) and anorthitic plagioclase (An ≥ 80). In contrast, fractionated (Mg# ≤ 60) lavas have Fe-rich olivine ($Fo_{75–84}$) coexisting with two kinds of clinopyroxene (endiopside–diopside with Mg# ≥ 80 and augite with Mg# < 80) and plagioclase (An ≥ 80 and An < 80). Reverse and oscillatory zoning is only observed in more fractionated plagioclase (An < 80 in the core), suggesting magma mixing perhaps in a magmatic reservoir. Fine-grained gabbro and diabase have Mg-rich clinopyroxenes (Mg# ≥ 60) coexisting with more albitic plagioclase (An ≤ 70). The mineral composition of the Toto caldera lavas and MGR lavas are within the compositional range of SEMFR lavas. Occurrence of two mineral compositional groups in Toto and MGR lavas, without significant compositional overlap, strongly suggests magma mixing (Supporting Information S4.2 and Fig. S4.1).

Olivine xenocrysts (≥0.5 mm) enclosing chromium spinel are common in primitive lavas (Figs 3c,5e). Olivine xenocrysts have higher Fo contents ($Fo_{89–92}$ core and $Fo_{87–97}$ rim) than do the olivine phenocrysts ($Fo_{86–88}$, Table S4.3 and Fig. S4.1 in Supporting Information) in their host basalts. Olivine xenocrysts host chromium spinel with Cr# (= 100 × Cr/(Cr + Al)) = 47–73. The olivine–spinel assemblages plot in the mantle array of Arai (1994) and they are similar to thoseof the SE Mariana forearc mantle peridotite (Cr# > 50 and $Fo_{90–92}$, Ohara & Ishii 1998), suggesting that these xenocrysts are samples of forearc mantle (Fig. 5c).

^{40}AR-^{39}AR AGES

Four SEMFR samples (two samples from Shinkai 6500 dive 1096, one sample each from Shinkai 6500 dive 1230 and YKDT-88) were dated by step-heating $^{40}Ar–^{39}Ar$ (Fig. 6 and Table 1). Initial $^{40}Ar–^{36}Ar$ for these samples (290–295) is nearly atmospheric ($^{40}Ar–^{36}Ar_{atmosphere}$ = 298.6), indicating that negligible radiogenic ^{40}Ar was inherited. Dated samples from dive 1096 samples include one from each of the lower (1096-R2) and upper series (1096-R16) lavas. These gave indistinguishable plateau ages of 3.5 ± 0.4 Ma (lower series 1096-R2) and 3.7 ± 0.3 Ma (upper series 1096-R16). Shinkai dive 1230 and YKDT-88 gave slightly younger ages, respectively of 2.8 ± 0.5 Ma and

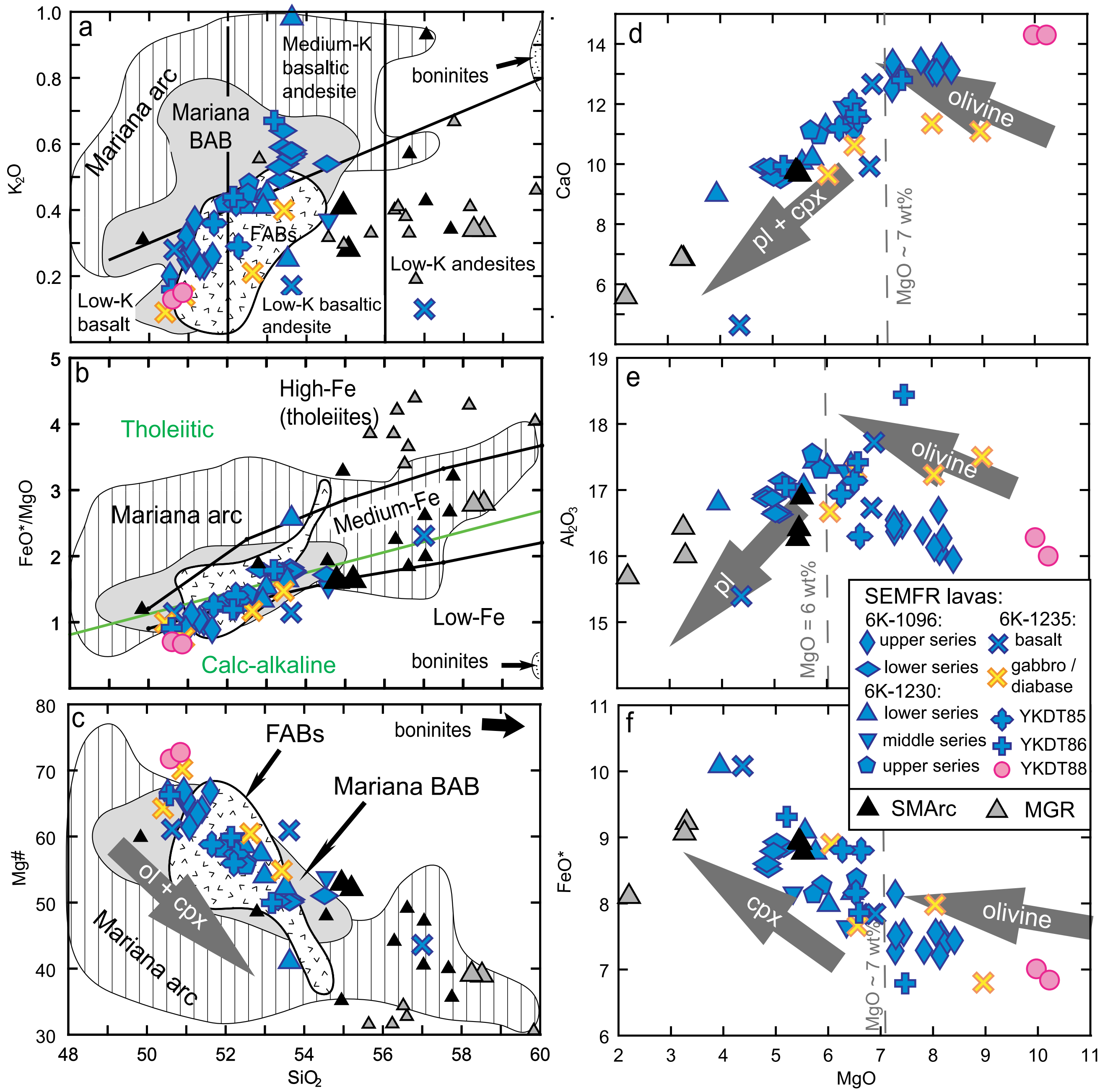

Fig. 4 Major element compositional characteristics of SEMFR, MGR, Eocene forearc basalts (FABs; Reagan *et al.* 2010), S. Mariana Arc lavas (SMArc: 13°10'N–11°N) which include Toto caldera lavas. All data recalculated to 100% anhydrous. (a) Potash-silica diagram (Peccerillo & Taylor 1976), showing that SEMFR lavas are low-K basalts to medium-K basaltic andesites. The grey field represents Mariana Trough BAB lavas (Hawkins *et al.* 1990; Gribble *et al.* 1996; Pearce *et al.* 2005; Kelley & Cottrell 2009) and the hatched field represents Mariana Arc lavas (Pearce *et al.* 2005; Wade *et al.* 2005; Stern *et al.* 2006; Shaw *et al.* 2008; Kelley & Cottrell 2009; Kelley *et al.* 2010). The small grey triangles are Malaguana–Gadao Ridge (MGR) data from Kakegawa *et al.* (2008) and Pearce *et al.* (2005). The small black triangles are data from SMA volcanoes (Kakegawa *et al.* 2008; Stern *et al.* 2013). Larger grey triangles denote MGR and larger black triangles denote Toto samples reported in this manuscript. The field for boninites is from Reagan *et al.* (2010). Note that SEMFR lavas mostly plot in field of Mariana Trough BAB lavas. (b) FeO*/MgO vs SiO_2 diagram for medium-Fe, medium-Fe, high-Fe discrimination (Arculus 2003); green line discriminates between tholeiitic and calk-alkaline lavas (Miyashiro 1974). (c) Mg# vs SiO_2 and (d) CaO, (e) Al_2O_3, (f) FeO* plotted against MgO for SEMFR, MGR, and Toto caldera. When plagioclase starts crystallizing, it produces a hinge in the liquid line of descent (LLD) of Al_2O_3. The hinge in Al_2O_3 is observed at MgO = 6 wt%; and the kink in CaO and FeO* is observed at MgO ~7 wt%. Therefore. primitive lavas are identified with MgO ≥ 7 wt%, following the method of Kelley *et al.* (2010). Arrows represent fractionation trends. Ol: olivine, pl: plagioclase, cpx: clinopyroxene. We used the same method as for SEMFR lavas (MgO ≥ 7 wt%) to filter the Mariana arc and Mariana Trough lavas.

Table 2 Overview of mean mineral compositions in samples from each dive in the SE Mariana Forearc Rift (SEMFR), Malaguana–Gadao Ridge (MGR) and Toto caldera

Sample #		Location	olivine xenocrysts n/s	Fo≥ 90	stdev	olivine n/s	Fo	stdev	feldspars n/s	An > 80	stdev	n/s	80 > An > 60	Stdev	n/s	An < 60	stdev	clinopyroxene n/s	Mg# ≥ 80	stdev	n/s	Mg# < 80	stdev
1096-R21	upper series	SEMFR	30/4	c: 92.6	0.3	22/7	c: 87.2	0.5	17/5	c: 81.7	1.1							26/12	c: 86.5	1.9			
	primitive basalt		6/4	r: 92.3	0.5	10/5	r: 86.5	0.4	4/2	r: 81.0	0.1							13/8	r: 86.9	0.8			
			3/2	r: 87.6	1.7																		
1096-R15	upper series	SEMFR				11/4	c: 86.8	1.1	19/8	c: 80.7	1.3							25/12	c: 87.6	0.9			
	primitive basalt					5/3	r: 85.7	1.2	8/4	r: 81.2	0.6							11/7	r: 87.6	0.5			
1096-R8	lower series	SEMFR				23/8	c: 76.9	2.1	2/1	*c: 84.7*	*0.3*	18/7	c: 67.9	3.3				13/4	c: 81.2	0.9	22/5	c: 76.8	2.4
	andesitic basalt					14/7	r: 76.5	1.0	2/1	*r: 87.7*	*0.1*	11/6	r: 68.4	1.6				9/4	r: 79.2	1.3	9/5	r: 76.6	3.0
1096-R4	lower series	SEMFR				15/7	c: 77.5	1.6		***c: 80.6***	***2.0***	**13/6**	c: 67.3	2.1				3/1	c: 81.5	0.6	26/8	c: 76.9	1.7
	andesitic basalt					8/4	r: 76.6	0.4	8/3	***m: 86.8***	***0.4***	**7/4**	r: 67.4	1.9				2/1	r: 82.8	0.4	13/8	r: 77.9	1.4
									4/2	***r: 83.4***	***0.4***												
1230-R14	lower series	SEMFR										12/8	c: 73.5	3.2				16/8	*c: 82.8*	*1.2*	*3/3*	c: 78.55	0.8
	basalt						NA											2/1	*r: 83.7*	*0.3*			
1230-R17	middle series	SEMFR							5/1	c: 91.3	0.4	8/3	c: 74.8	2.1				18/7	*c: 85.0*	*2.2*	3/3	c: 75.59	1.4
	basalt						NA		4/1	m: 84.5	3.8							3/1	*r:87.0*	*0.9*			
									4/1	st: 85.7	2.9												
									5/1	r: 86.4	1.8												
1230-R26	upper series	SEMFR				7/3	c: 82.5	1.0	20/7	**c: 86.9**	**3.1**	**5/2**	c: 75.0	0.2				8/5	c: 83.3	1.9	8/5	*c: 74.8*	*2.1*
	basalt					2/1	r: 83.3	0.1	12/4	**m: 82.4**	**4.5**							4/2	r: 83.6	0.8	3/2	*m: 81.8*	*3.1*
									13/6	**r: 77.7**	**3.7**										5/2	*r: 85.6*	*0.4*
1235-R11	Diabase	SEMFR													3/3	c: 20.5	2.3	4/4	c: 88.0	1.1			
															3/3	c: 47.9	6.5	3/3	r: 76.0	1.4			
															1/1	r: 35.9	–	2/2	c: 82.4	0.5			
																		2/2	r: 85.9	2.3			
1235-R12	diabasic basalt	SEMFR				3/1	c: 89.0	0.2	8/4	c: 80.8	2.9							5/3	**c: 84.6**	**1.1**			
						1/1	r: 86.0	–	8/4	r: 73.1	6.6							4/3	**r: 86.1**	**0.6**			
																		5/3	**r: 74.7**	**2.9**			
	basaltic enclave					3/1	c:* 85.2	1.4				6/5	c: *63.1	4.7				5/2	c*: 85.5	0.4	2/2	gr*: 74.9	2.3
																		4/2	r*: 81.9	2.4			
1235-R13	diabasic gabbro	SEMFR										2/2	c: 64.6	7.5	**8/4**	**c: 23.6**	**9.8**	14/7	c: 84.2	0.9	2/2	c: 76.5	3.8
															2/1	**m: 57.7**	**1.5**	6/4	r: 83.7	2.0	4/3	r: 73.4	1.6
															2/1	**r: 40.4**	**5.9**						
															1/1	**r: 15.8**	**–**						
85-R7	basalt	SEMFR				7/4	c: 83.4	0.8	2/1	c: 82.1	2.4	13/5	c: 74.7	1.4				8/5	c: 85.6	0.6			
									2/1	r: 75.8	2.4	6/3	r: 75.4	3.7				8/4	r: 83.5	0.3			
86-R20	basalt	SEMFR				3/2	c: 76.0	1.1	6/4	c: 84.4	1.7	3/3	c: 79.9	0.2				14/4	*c: 82.2*	*1.5*			
									2/2	r: 83.5	0.8	2/2	r: 72.5	1.3				6/3	*r: 83.0*	*0.7*			
88-R1	basalt	SEMFR	26/7	c: 89.9	0.9	11/5	gr: 86.9	0.5	14/6	c: 89.7	0.7							17/7	c: 89.7	1.5			
			11/7	r: 89.5	0.6				4/2	r: 89.2	0.3							6/3	r: 88.7	2.3			
164-3R	Andesite	MGR							5/2	c: 86.4	0.1	2/1	gr: 52.3	2.7				4/2	c: 87.4	0.1			
																		3/2	r: 85.0	1.5			
163-1-3R	Andesite	Toto caldera							14/6	***c: 86.5***	***3.0***	**1/1**	***c: 72.0***								2/1	c: 78.2	0.6
									5/12	***r: 88.6***	***0.6***	**2/2**	***r: 74.0***	5.5							2/1	r: 77.6	0.3
																					2/1	gr: 73.6	1.1
163-3-4R	Andesite	Toto caldera					NA					18/6	c: 76.4	2.1				6/2	c: 81.1	0.3	1/1	gr: 78.7	0.7
							NA					10/5	r: 72.9	2.7				4/2	r: 81.8	0.4			

n, the total number of analyses performed in one sample; s, the number of minerals analyzed in each sample; c, core; m, mantle; st, sieve texture; r, rim; gr, groundmass; * minerals in 1235-R12 observed in the microcrystallized basalt, while the other 1235-R12 analyses refer to minerals in the diabasic xenolith. Numbers in italics represent reverse zoning. Bold numbers represent minerals with oscillatory zoning. NA, not analyzed; MGR, Malaguana–Gadao Ridge; SEMFR, SE Mariana Forearc Rift.

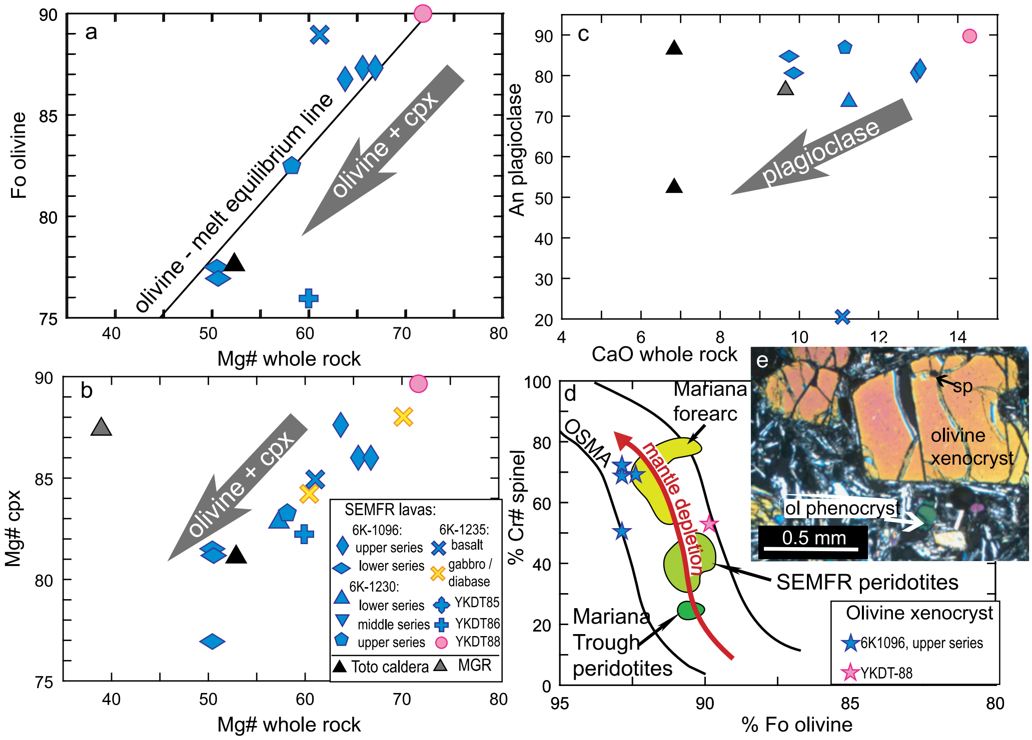

Fig. 5 Variation of (a) olivine Fo and (b) clinopyroxene Mg# composition with whole rock Mg#. (c) Variation of An content of plagioclase core with whole rock CaO (wt%) content. Olivine, clinopyroxene and plagioclase are mostly in equilibrium with their host rock. Fractional crystallization (grey arrow) removes Mg-rich minerals from the residual melt which precipitates increasingly Fe-rich minerals. The olivine-liquid equilibrium line is calculated from experimental data of Roeder and Emslie (1970) with K_D olivine – melt = 0.3 and $Fe^{3+}/Fe_T = 0.17$ (Kelley & Cottrell 2009). (d) Olivine–Spinel Mantle Array (OSMA) diagram of Arai (1994). Cr# of spinel inclusions and Fo content of host olivine xenocrysts in Shinkai dive 1096 upper series (blue star) and in YKDT-88 lavas (pink stars) plot within OSMA. Cr# are means for each spinel inclusion and reported with the Fo content of their olivine host. Their Cr# ≥ 50 is similar to that of the southern Mariana forearc peridotite (Ohara & Ishii 1998); whereas BAB peridotites have Cr# < 30 (Ohara *et al.* 2002). SEMFR peridotites (Michibayashi *et al.* 2009; Sato & Ishii 2011) have Cr# and Fo contents intermediate between southern Mariana forearc peridotites and Mariana Trough BAB peridotites (Ohara *et al.* 2002). (e) Large xenocryst of anhedral olivine (ol) with Fo_{90-92} hosting chromium spinel (sp) from sample YKDT88-R2.

2.7 ± 0.3 Ma. The SEMFR ^{40}Ar–^{39}Ar ages indicate that seafloor spreading occurred in Pliocene time (Fig. 1b), and suggest that the SEMFR seafloor youngs toward the MGR.

DISCUSSION

GENESIS OF SEMFR LAVAS

Compositions of lavas and their minerals record the conditions of magma genesis and evolution; and from this, important tectonic information can be gleaned (e.g. Klein & Langmuir 1987). Incompatible elements such as K_2O, Na_2O and TiO_2 are concentrated in the melt as mantle melting or crystal fractionation proceeds. The first melt fraction is enriched in these elements and so concentrations anti-corrrelate with fraction of melting, or 'F' (Klein & Langmuir 1987; Taylor & Martinez 2003; Kelley *et al.* 2006, 2010). In addition, K_2O contents in convergent margin magma sources are strongly affected by subduction-related metasomatism (e.g. K-h relationship, Dickinson 1975; Kimura & Stern 2008), therefore this element is generally not used to monitor F. FeO contents in basalts also contain petrogenetic information. In basaltic systems, deeper melts are progressively enriched in iron (Klein & Langmuir 1987). Therefore, the Na_2O, TiO_2 and FeO contents of lavas are good proxies for the degree and depth of melting. However, estimating the extent and depth of partial melting requires primitive lavas with compositions in equilibrium with their mantle source. Consequently, Na_2O, TiO_2 and FeO contents are commonly corrected for olivine fractionation in order to infer their Na_8, Ti_8 and Fe_8 contents (Na_2O, TiO_2, and FeO contents calculated at MgO = 8 wt%). The Na_8 of N-MORBs anti-correlates with Fe_8, indicating that melting is

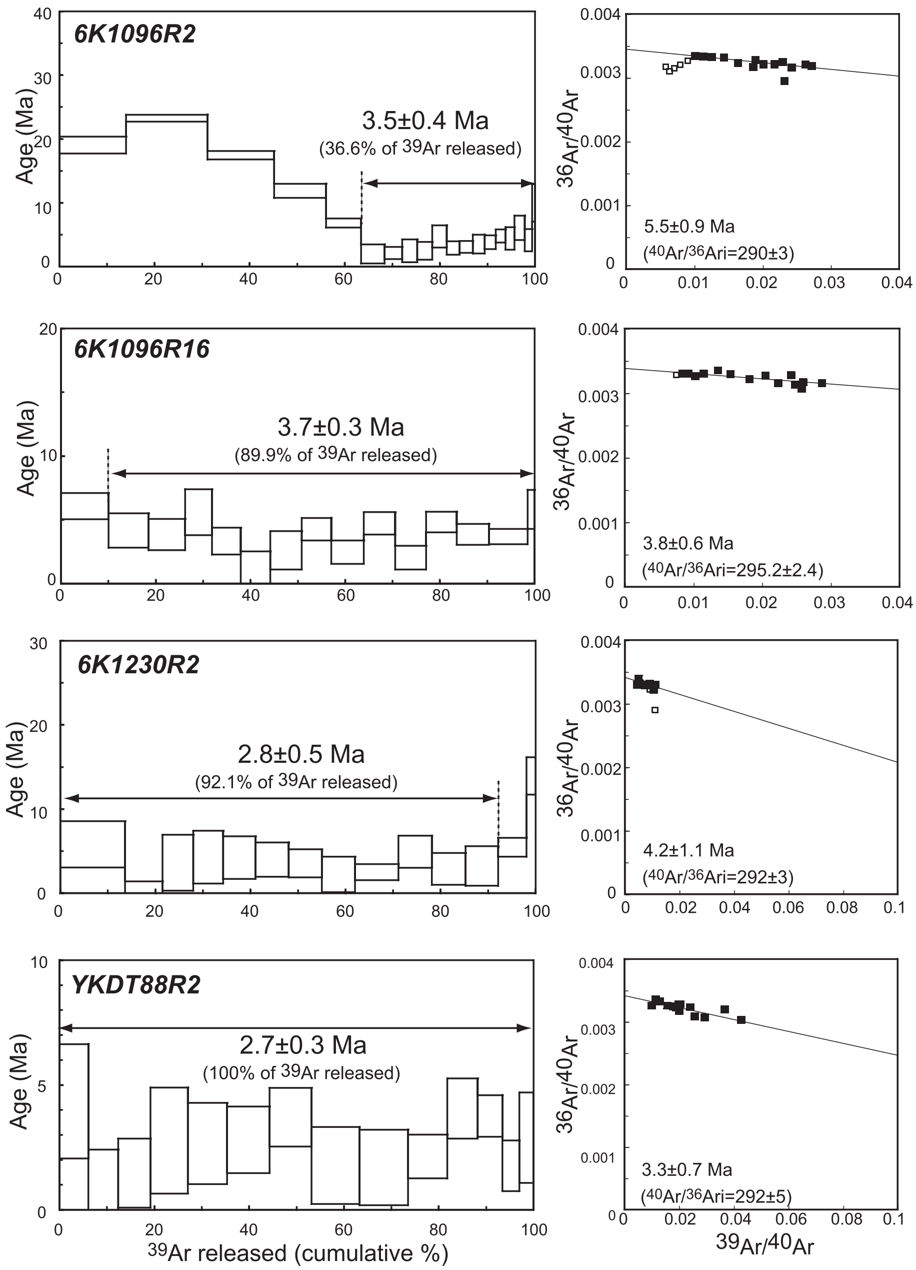

Fig. 6 The ^{40}Ar–^{39}Ar age spectra with ^{36}Ar–^{40}Ar vs ^{39}Ar–^{40}Ar plot for samples from the SEMFR. Percentage of ^{39}Ar released during analysis is also reported.

greater if it begins deeper (Fig. 7a; Klein & Langmuir 1987; Arevalo Jr. & McDonough 2010). Subduction-related melting is somewhat different because melting extents are enhanced by water (Gribble *et al.* 1996; Taylor & Martinez 2003; Kelley *et al.* 2006). BAB magma sources often are affected by subducted water and are characterized by more melting at shallower depth than MORBs, so that Na_8 increases with Fe_8 (Fig. 7a; Taylor & Martinez 2003; Kelley *et al.* 2006). BAB and arc lavas have distinct geochemical signatures (Fig. 7), resulting from elements dissolved in fluids derived from the subducting slab that are involved in magma genesis. Arc lavas have lower Na_8 and Ti_8 contents at higher K_2O/TiO_2 and Fe_8 content because they formed by high degrees of melting at greater depths in the presence of slab-derived fluids. In contrast, BAB lavas have higher Na_8 and Ti_8 contents at lower K_2O/TiO_2 and Fe_8 content, as they were generated at shallower depth by adiabatic mantle decompression, with less involvement of slab-derived fluids.

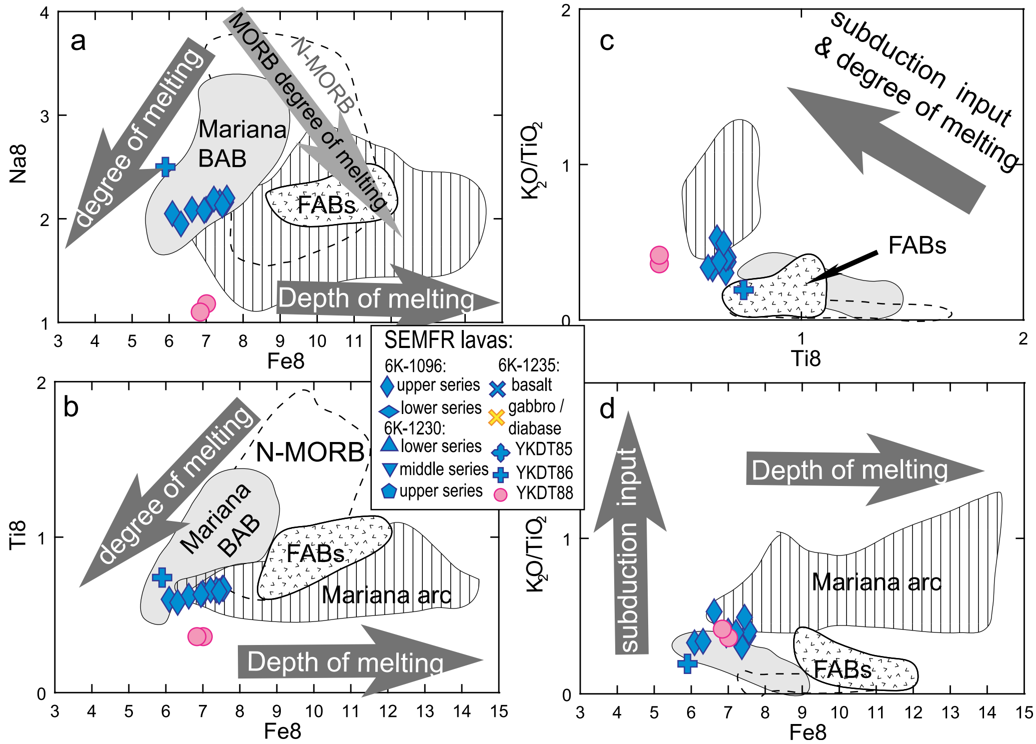

Fig. 7 Diagrams showing variations in (a) Na_8, (b) Ti_8, (d) K_2O/TiO_2 versus Fe_8 and (c) K_2O/TiO_2 versus Ti_8. Na_8 and Ti_8 are proxies for the fraction of mantle that is melted, Fe_8 is a proxy for the depth of mantle melting (Klein & Langmuir 1987), and K_2O/TiO_2 is a proxy for the subduction input. The grey field represents Mariana Trough BAB lavas (Hawkins *et al.* 1990; Gribble *et al.* 1996; Pearce *et al.* 2005; Kelley & Cottrell 2009) and the hatched field represents Mariana arc lavas (Pearce *et al.* 2005; Wade *et al.* 2005; Stern *et al.* 2006; Shaw *et al.* 2008; Kelley & Cottrell 2009; Kelley *et al.* 2010). Primitive lavas from the Mariana Trough and the Mariana arc were filtered as SEMFR lavas (MgO ≥ 7 wt%) for consistency. The FABs field is from Reagan *et al.* (2010). The negative correlation of Na_8 with Fe_8 of N-MORBs (grey arrow; Arevalo Jr. & McDonough 2010) shows that more magma is produced when melting begins deeper; while in subduction-related lavas, more melting is produced shallower. SEMFR lavas have Na_8 and Ti_8 contents slightly varying with Fe_8 content, indicating homogeneous degree of mantle melting.

To investigate SEMFR magmagenesis (i.e. whether SEMFR lavas were produced in BAB-like and/or in arc-like magmagenetic settings), we calculated Na_8, Ti_8 and Fe_8 contents for these lavas. Plots of Al_2O_3, CaO and FeO* against MgO (Fig. 4d-f) show that the kinks in Al_2O_3 and CaO, indicating the beginning of plagioclase and clinopyroxene crystallization, are respectively observed at MgO = 6 wt% and at MgO ~7 wt%. Therefore, data were filtered to exclude highly fractionated samples with MgO < 7 wt% that crystallized olivine, clinopyroxene, and plagioclase on their LLD (Fig. 4d-f), following the method described in Kelley *et al.* (2006) and Kelley *et al.* (2010). The least fractionated samples with 7–8 wt% MgO, which fractionated olivine only (Fig. 4d-f), were then corrected to MgO = 8 wt% using the equations of Klein and Langmuir (1987) for Na_8 and Fe_8, and Taylor and Martinez (2003) for Ti_8. These are listed in Table 1 (mean SEMFR Na_8 = 1.99 ± 0.40 wt% (1 std. dev.); mean Ti_8 = 0.60 ± 0.11 wt%;. mean Fe_8 = 6.91 ± 0.54 wt%). The Na_8, Fe_8 and Ti_8 contents of SEMFR lavas are slightly lower than those observed for N-MORBs (Arevalo Jr. & McDonough, 2010), indicating that higher degrees of mantle melting were produced at shallower depths. The SEMFR lavas have similar Ti_8 and Na_8 contents at lower Fe_8 than FABs; and they plot in the compositional overlap between Mariana arc lavas and the Mariana BAB lavas, with homogeneous, low Na_8 and Ti_8 contents varying little with Fe_8 content (Fig. 7a-b), suggesting a roughly constant degree and depth of mantle melting. These lavas were produced by extensive melting (≥15%) of shallow mantle (~25 ± 6.6 km, see the section entitled Pressure and Temperature of Mantle Melting). The K_2O/TiO_2 (proxy for the total subduction input; Shen & Forsyth 1995) of SEMFR lavas is higher that of FABs and plot between the arc–BAB compositional fields (Fig. 7c-d), well above N-MORBs, further demonstrating a subduction component in SEMFR magma genesis. Only lavas from YKDT-88, collected closest to the FNVC (Fig. 1b), do not plot on

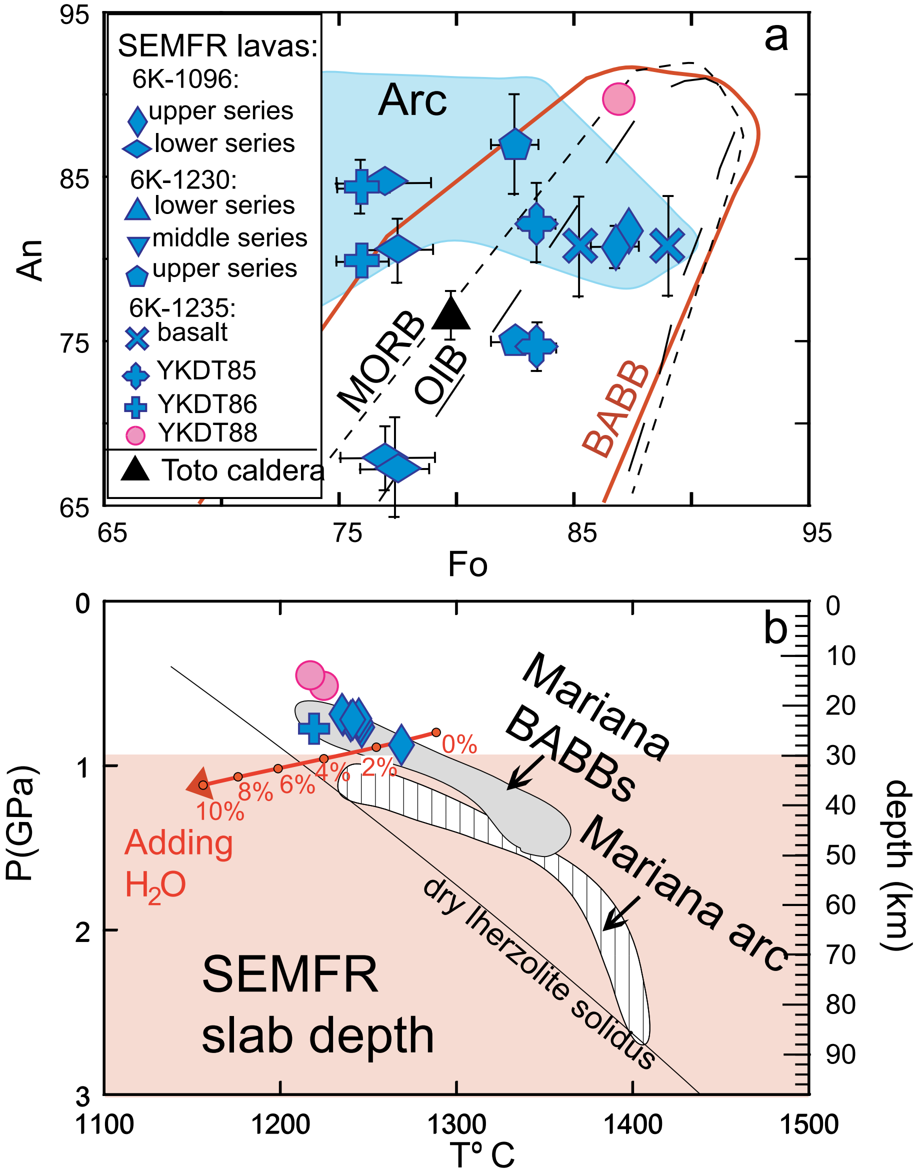

Fig. 8 (a) Composition ranges for coexisting olivine Fo–plagioclase An in intraoceanic arc lavas (blue field) and BABB (red outline) after Stern *et al.* (2006). Arc basalts have more calcic plagioclase in equilibrium with more Fe-rich olivine compared to MORB (short dashed outline), OIB (long dashed outline), and BABB. The plagioclase-olivine relationships of SEMFR lavas generally plot in the overlap between the BABB and the arc composition fields. The black triangle denotes a Toto caldera sample. (b) P–T conditions of mantle-melt equilibration estimated by using the procedure of Lee *et al.* (2009) for SEMFR primitive lavas with MgO ≥ 7 wt%. Also shown are Mariana Trough basaltic glasses (Gribble *et al.* 1996; Kelley & Cottrell 2009), and the Mariana arc melt inclusions with analyzed water contents (Shaw *et al.* 2008; Kelley *et al.* 2010). The solidus is from Katz *et al.* (2003). We used $Fe^{3+}/Fe_{t} = 0.17$ for SEMFR and Mariana Trough BABBs, $Fe^{3+}/Fe_{t} = 0.25$ for Mariana arc lavas (Kelley & Cottrell 2009) and Fo_{90} for the equilibrium mantle. We used the same method as for SEMFR lavas (MgO ≥ 7 wt%) to filter the Mariana arc and Mariana Trough glass for consistency. The pink field represents the slab depth beneath SEMFR (≤30 km–100 km depth; Becker 2005).

the SEMFR compositional field (Fig. 7a-c), with lower Na_8 and Ti_8 at similar Fe_8 contents. Their Ti_8 and Na_8 values are lower than those of Mariana arc lavas (Fig. 7a-c), suggesting that YKDT-88 lavas were produced by more mantle melting and/or melting of a more depleted mantle source at similar depth compared to other SEMFR magmas.

The above inference that SEMFR lavas are similar to backarc basin basalts (BABB) can be checked by examining mineral compositions, because arc basalts and BABBs have distinct An-Fo relationships (Stern 2010). Arc basalts contain more Fe-rich olivine with more An-rich plagioclase compared to BABB, MORB, and OIB (Ocean Island Basalt, Fig. 8a) because higher water contents in arc magmas delay plagioclase but not olivine crystallization (Kelley *et al.* 2010; Stern 2010), resulting in higher CaO and FeO contents in the melt when plagioclase starts crystallizing. In contrast, BABBs, formed largely by adiabatic decompression mantle melting, have Fo-An relationships essentially indistinguishable from those of MORB and OIB (Fig. 8a). Accordingly, we can discriminate arc basalts from BABBs based on An and Fo contents of the plagioclase–olivine assemblages. Figure 8a shows that most SEMFR lavas plot within the BABB compositional field, consistent with observations from Na_8, Ti_8, and Fe_8 discussed in the previous section. Some samples also plot within the arc compositional field, strongly suggesting that BAB-like (i.e. adiabatic decompression melting) and arc-like (i.e. wet mantle melting) conditions of magmagenesis coexisted beneath SEMFR. We propose that SEMFR magmas formed by adiabatic decompression of fertile asthenospheric mantle (BAB-like mantle) metasomatized by slab-derived fluids, enriching the melt in water and sometimes delaying plagioclase fractionation.

PRESSURE AND TEMPERATURE OF MANTLE MELTING

The P–T conditions of mantle melting, recorded by primary melts in equilibrium with the mantle beneath SEMFR, were calculated from major element compositions of primitive basalts with $MgO \geq 7$ wt% (Kelley *et al.* 2010; Fig. 4d-f) by using the geothermobarometer of Lee *et al.* (2009), based on Si, Mg and water contents of primitive magmas. The estimated P–T conditions are those of the last melt in equilibrium with the mantle or a mean value of the P–T conditions of polybaric, fractional pooled melts recorded along a melting column (Kelley *et al.* 2010). SEMFR lavas are compositionally similar to BABBs, we therefore used BAB-like oxidation state ($Fe^{3+}/Fe_T = 0.17$) and averaged Mariana BAB water content (1.31 wt%; Gribble *et al.* 1996; Kelley & Cottrell 2009) for SEMFR lavas, $Fe^{3+}/Fe_T = 0.17$ for Mariana Trough lavas and $Fe^{3+}/Fe^T = 0.25$ for Mariana arc magmas (Kelley & Cottrell 2009). We also used lherzolitic BAB-like mantle source (Fo_{90}; Kelley *et al.* 2006) to estimate the P–T conditions of SEMFR mantle melting. Primitive lavas of the Mariana Trough and the Mariana arc with analyzed water were filtered for $MgO \geq 7$ wt% as SEMFR lavas for consistency. SEMFR whole rock compositions indicate melting pressures of 0.5–0.9 GPa (± 0.2 GPa) and temperatures of 1217–1269°C (± 40°C), with a mean of 0.7 ± 0.2 GPa (~23 ± 6.6 km) and 1239 ± 40°C (Fig. 8b). This is consistent with melting just above the present subducting slab (≤30–100 km depth), although we do not know the position of the subducting slab at 2.7–3.7 Ma, when SEMFR melts were generated. Mariana Trough BABBs (Gribble *et al.* 1996; Kelley & Cottrell 2009) have similar P–T conditions of mantle melting (0.7–1.5 ± 0.2 GPa, 1214–1359 ± 40°C; mean melting depth ~33 ± 6.6 km). In contrast, Mariana arc lavas (Shaw *et al.* 2008; Kelley *et al.* 2010) show higher P–T conditions of mantle melting (1.1 – 3.0 ± 0.2 GPa, 1240 – 1522 ± 40°C). These results suggest that SEMFR lavas and Mariana Trough BABBs were similarly generated by adiabatic decompression of shallow asthenospheric mantle (~25–30 ± 6.6 km). In contrast, arc lavas (Shaw *et al.* 2008; Kelley & Cottrell 2009; Kelley *et al.* 2010) recorded deeper (mean melting depth ~51 ± 6.6 km) and hotter mantle melting conditions (Kelley *et al.* 2010). This leads to the further deduction that SEMFR lavas formed by BABB-like seafloor spreading at 2.7 to 3.7 Ma.

GEODYNAMIC EVOLUTION OF THE SOUTHEASTERN MARIANA FOREARC RIFT

Investigations of the petrography and geochemistry of SEMFR lavas reveal that: (i) SEMFR lavas are petrographically and compositionally similar to Mariana Trough BABBs; (ii) SEMFR melts interacted with the pre-existing forearc lithosphere and picked up some forearc mantle olivines, indicating rapid ascent; (iii) magmatic activity (2.7–3.7 Ma) formed SEMFR oceanic crust by seafloor spreading (no Eocene forearc basement has been recovered from the SEMFR); (iv) SEMFR primitive basalts formed by decompression melting at ~23 km depth and 1239°C, like that associated with the Mariana Trough backarc basin, suggesting similar formation; and (v) lack of evidence for recent igneous and hydrothermal activity, except near MGR and the Toto caldera, indicates that the presently-observed NNW–SSE trending relief formed during post-magmatic rifting (<2.7 Ma).

The SEMFR is a rift with no morphological expression of large arc-like volcanoes, like those of the Mariana arc. SEMFR lavas are vesicular with K_2O contents (Fig. 4a) and K_2O/TiO_2 ratios that are similar to MGR and other Mariana Trough BAB lavas (Fig. 7c,d). They also have similar P–T conditions of magma genesis, demonstrating that they formed by adiabatic decompression of BAB-like

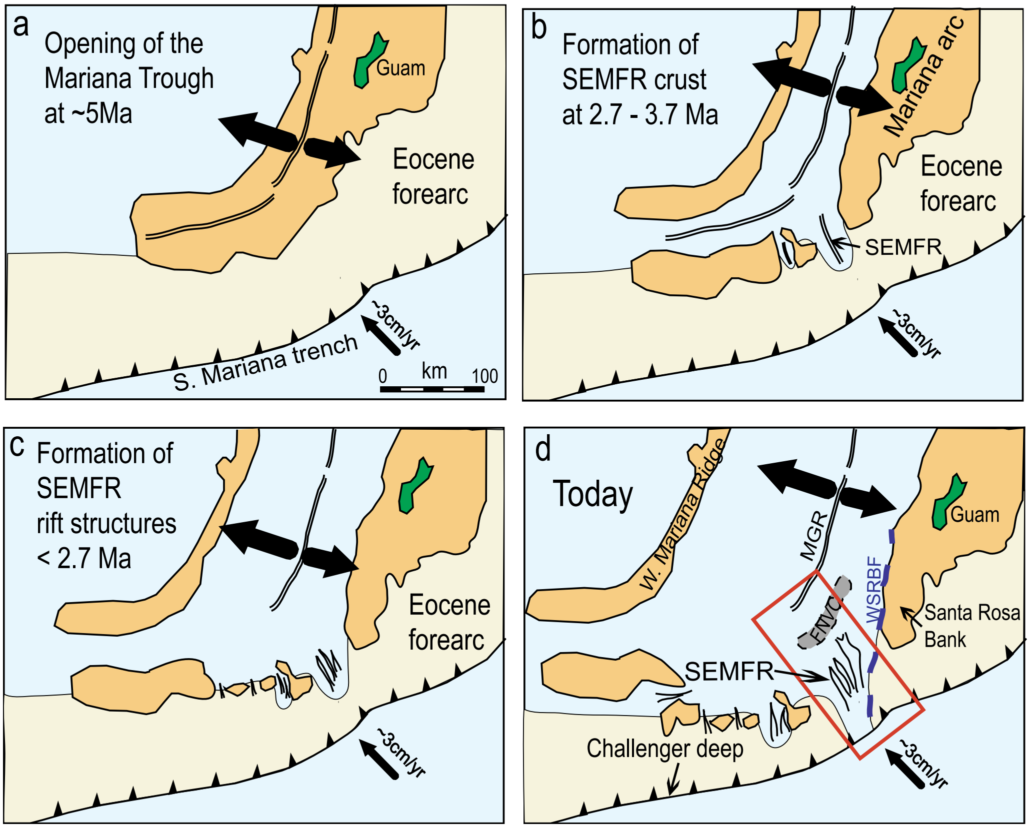

Fig. 9 Geodynamic evolution of SEMFR. (a) The Mariana Trough is opening ~5 Ma. (b) Spreading of the Mariana Trough rifts the arc lithosphere (in orange) and forms SEMFR by stretching the forearc crust (in yellow) ~2.7–3.7 Ma. We speculate that SEMFR is a spreading center with intense magmatic activity. (c) Post-magmatic deformation of SEMFR occurred < 2.7 Ma, and intensely deformed the Eocene forearc crust. (d) Today, SEMFR is no longer magmatically active and amagmatic extension dominates the rift. Eocene forearc is eroded with opening of the S. Mariana Trough. Actual position of the forearc is based on R/V Yokosuka YK08-08 Leg 2 and YK10-12 cruise reports (Ohara *et al.* 2008, 2010). The red box highlights the area of Figure 10.

mantle metasomatized by slab-derived fluids. These observations raise a fundamental question: were SEMFR lavas produced by seafloor spreading in the backarc basin or in the forearc? The southernmost Mariana convergent margin has reorganized rapidly since its collision with the Caroline Ridge, suggesting that SEMFR lavas were produced by different geological settings from those that exist today. From the location of the SEMFR adjacent to the trench, it is clear that these lavas formed in the forearc. We propose a geodynamic model for the southernmost Mariana arc, in which SEMFR formed to accommodate opening of the southernmost Mariana Trough (Fig. 9a,b and Fig. 10a-c). Rupturing the forearc lithosphere allowed asthenospheric mantle to flow into the forearc and to melt by adiabatic decompression under hydrous conditions at 2.7–3.7 Ma; and origin of the SEMFR mantle (i.e. from the backarc basin, the arc, or a slab window) is still under investigation. Some SEMFR melts picked up fragments of pre-existing forearc mantle during ascent, demonstrating that SEMFR lavas formed long after subduction initiation. Post-magmatic activity (<2.7 Ma) shapes the S. Mariana forearc lithosphere (Fig. 9c) and formed the NNW–SSE trending rifts of the SEMFR, as we know it today (Figs 9d,10d).

CONCLUSIONS

Two important conclusions can be drawn from this study: (i) SEMFR magmas formed by adiabatic decompression in the southernmost IBM forearc, usually underlain by cold, serpentinized harzburgitic mantle that rarely melts (Reagan *et al.* 2010); and (ii) SEMFR lavas were produced by melting of fertile asthenospheric mantle metasomatized by slab-derived fluids, long after subduction initiation, allowing development of a forearc lithosphere. Our results show that the southernmost Mariana forearc stretched to accommodate opening of the Mariana Trough to form the SEMFR, allowing

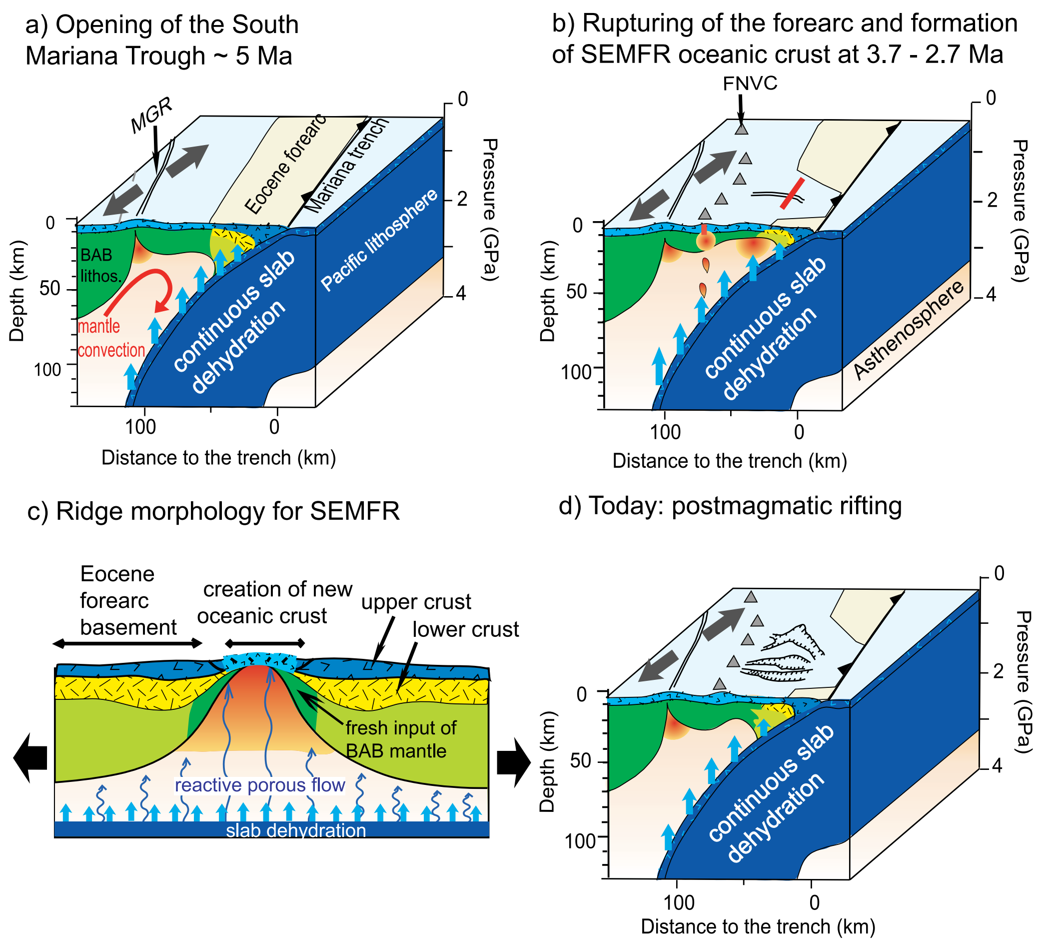

Fig. 10 3D model of geodynamic evolution of the SEMFR drawn after the SE Mariana lithospheric section of Gvirtzman and Stern (2004) and the tomographic images of Miller *et al.* (2006a). The cross section is drawn from the area highlighted by a red box in Figure 9. BAB lithos., backarc basin lithosphere. (a) Opening of the S. MarianaTrough, the Malaguana–Gadao Ridge (MGR), stretches the pre-existing Eocene forearc lithosphere ~5 Ma ago. (b) Rupturing of the forearc allows mantle melting, creating new SEMFR oceanic crust ~2.7–3.7 Ma. The red line shows the location of the cross section of SEMFR shown in c. (c) Continuous dehydration of the shallow downgoing slab controlled SEMFR magmatic activity, and SEMFR had ridge morphology ~2.7–3.7 Ma. (d) Today, post-magmatic rifting dominates SEMFR.

hydrated, asthenospheric mantle to flow into the forearc and to produce new oceanic crust at ~2.7–3.7 Ma. SEMFR lavas formed by adiabatic decompression of depleted backarc mantle at ~23 ± 6.6 km depth and 1239 ± 40°C. The SEMFR at 2.7–3.7 Ma was likely a ridge-like spreading center, where the slab-derived fluids enhanced mantle melting beneath the forearc. Today, the SEMFR is no longer magmatically active and amagmatic extension shapes its morphology.

ACKNOWLEDGEMENTS

We thank JAMSTEC for providing Kaiko samples and related videos, Teruaki Ishii, Stuart Murchison, Katsuyoshi Michibayashi, Warren Lieu, Susumu Umino and two anonymous reviewers for their help and their insightful comments that improved this manuscript. Many thanks to the R/V Yokosuka crew for their efforts work during YK08-08 Leg 2 and YK10-12 cruises. This research was supported by NSF grant 0961352 to RJS. This is UTD Geosciences Contribution # 1246.

REFERENCES

ARAI S. 1994. Characterization of spinel peridotites by olivine-spinel compositional relationships: Review and interpretation. *Chemical Geology* **113**, 191–204.

ARCULUS R. J. 2003. Use and abuse of the terms calcalkaline and calcalkalic. *Journal of Petrology* **44**, 929–35.

AREVALO JR. R. & MCDONOUGH W. F. 2010. Chemical variations and regional diversity observed in MORB. *Chemical Geology* **271**, 70–85.

Baker E. T., Embley R. W., Walker S. L. *et al.* 2008. Hydrothermal activity and volcano distribution along the Mariana arc. *Journal of Geophysical Research* **113**, B08S09. doi: 10.1029/2005GC000948

Becker N. C. 2005. Recent volcanic and tectonic evolution of the southern Mariana arc (PhD thesis) pp. 166, University of Hawai'i, Hawai'i.

Becker N. C., Fryer P. & Moore G. F. 2010. Malaguana-Gadao Ridge: Identification and implications of a magma chamber reflector in the southern Mariana Trough. *Geochemistry Geophysics Geosystems* **11**, Q04X13. doi: 10.1029/2009GC002719

Bird P. 2003. An updated digital model of plate boundaries. *Geochemistry Geophysics Geosystems* **4**, 1027. doi:10.1029/2001GC000252

Bloomer S. H. & Hawkins J. W. 1983. Gabbroic and ultramafic rocks from the Mariana Trench: An island arc ophiolite. *In* Hayes D. E. (ed.) *The Tectonic and Geologic Evolution of Southeast Asian Seas and Islands: Part 2*, pp. 294–317, American Geophysical Union, Geophysical Monograph Series 27, Washington, DC.

Dickinson W. R. 1975. Potash-depth (K-h) relations in continental margin and intra-oceanic magmatic arcs. *Geology* **3**, 53–6.

Fryer P. 1993. The relationship between tectonic deformation, volcanism, and fluid venting in the southeastern Mariana convergent plate margin. *Proceedings of Jamstec, Symposium on Deep Sea Research* **9**, 161–79.

Fryer P., Becker N., Appelgate B., Martinez F., Edwards M. & Fryer G. 2003. Why is the Challenger Deep so deep? *Earth and Planetary Science Letters* **211**, 259–69.

Fryer P., Fujimoto H., Sekine M. *et al.* 1998. Volcanoes of the southwestern extension of the active Mariana island arc: New swath-mapping and geochemical studies. *Island Arc* **7**, 596–607.

Funiciello F., Faccenna C., Giardini D. & Regenauer-Lieb K. 2003. Dynamics of retreating slabs: 2. Insights from three-dimensional laboratory experiments. *Journal of Geophysical Research* **108**, 2207. doi: 10.1029/2001JB000896

Funiciello F., Moroni M., Piromallo C., Faccenna C., Cenedese A. & Bui H. A. 2006. Mapping mantle flow during retreating subduction: Laboratory models analyzed by feature tracking. *Journal of Geophysical Research* **111**, B03402. doi: 10.1029/2005JB003792

Gamo T., Masuda H., Yamanaka T. *et al.* 2004. Discovery of a new hydrothermal venting site in the southernmost Mariana Arc : Al-rich hydrothermal plumes and white smoker activity associated with biogenic methane. *Geochemical Journal* **38**, 527–34.

Gardner J. V. 2006. Law of the sea cruise to map the western insular margin and 2500-m Isobath of Guam and the Northern Mariana Islands. Cruise report. *Center for Coastal and Ocean Mapping (CCOM)/Joint Hydrographic Center (JHC)*, University of New Hampshire (UNH), Durham, NH.

Gardner J. V. 2007. U.S. law of the sea cruise to map the western insular margin and 2500-m Isobath of Guam and the Northern Mariana Islands. Cruise report. *Center for Coastal and Ocean Mapping (CCOM)/Joint Hydrographic Center (JHC)*, University of New Hampshire (UNH), Durham, NH.

Gardner J. V. 2010. U.S. Law of the Sea cruises to map sections of the Mariana Trench and the eastern and southern insular margins of Guam and the Northern Mariana Islands. Cruise report. *Center for Coastal and Ocean Mapping (CCOM)/Joint Hydrographic Center (JHC)*, University of New Hampshire (UNH), Durham, NH.

Gardner J. V. & Armstrong A. A. 2011. The Mariana Trench: A new view based on multibeam echosounding. *American Geophysical Union, Fall Meeting 2011*, abstract #OS13B-1517, San Fransisco.

Gribble R. F., Stern R. J., Bloomer S. H., Stüben D., O'hearn T. & Newman S. 1996. MORB mantle and subduction components interact to generate basalts in the southern Mariana Trough back-arc basin. *Geochimica et Cosmochimica Acta* **60**, 2153–66.

Gvirtzman Z. & Stern R. J. 2004. Bathymetry of Mariana trench-arc system and formation of the Challenger Deep as a consequence of weak plate coupling. *Tectonics* **23**, TC2011. doi: 10.1029/2003tc001581

Hawkins J. W., Lonsdale P. F., Macdougall J. D. & Volpe A. M. 1990. Petrology of the axial ridge of the Mariana Trough backarc spreading center. *Earth and Planetary Science Letters* **100**, 226–50.

Hulme S. M., Wheat C. G., Fryer P. & Mottl M. J. 2010. Pore water chemistry of the Mariana serpentinite mud volcanoes: A window to the seismogenic zone. *Geochemistry Geophysics Geosystems* **11**, Q01X09. doi:10.1029/2009gc002674

Hyndman R. D. & Peacock S. M. 2003. Serpentinization of the forearc mantle. *Earth and Planetary Science Letters* **212**, 417–32.

Ishizuka O., Tani K., Reagan M. K. *et al.* 2011. The timescales of subduction initiation and subsequent evolution of an oceanic island arc. *Earth and Planetary Science Letters* **306**, 229–40.

Kakegawa T., Utsumi M. & Marumo K. 2008. Geochemistry of sulfide chimneys and basement pillow lavas at the Southern Mariana trough (12.55°N and 12.58°N). *Resource Geology* **58**, 249–66.

Kato T., Beavan J., Matsushima T., Kotake Y., Camacho J. T. & Nakao S. 2003. Geodetic evidence of back arc spreading in the Mariana trough. *Geophysical Research Letters* **30**, 1625. doi:10.1029/2002GL016757

Katz R. F., Spiegelman M. & Langmuir C. H. 2003. A new parameterization of hydrous mantle melting. *Geochemistry Geophysics Geosystems* **4**, 1073. doi: 10.1029/2002GC000433

KELLEY K. A. & COTTRELL E. 2009. Water and the oxidation state of subduction zone magmas. *Science* **325**, 605–7.
KELLEY K. A., PLANK T., GROVE T. L., STOLPER E. M., NEWMAN S. & HAURI E. 2006. Mantle melting as a function of water content beneath back-arc basins. *Journal of Geophysical Research* **111**, B09208. doi: 10.1029/2005jb003732
KELLEY K. A., PLANK T., LUDDEN J. & STAUDIGEL H. 2003. Composition of altered oceanic crust at ODP Sites 801 and 1149. *Geochemistry Geophysics Geosystems* **4**, 8910. doi: 10.1029/2002GC000435
KELLEY K. A., PLANK T., NEWMAN S. *et al.* 2010. Mantle melting as a function of water content beneath the Mariana Arc. *Journal of Petrology* **51**, 1711–38.
KIMURA J.-I. & STERN R. J. 2008. Neogene volcanism of the Japan Island Arc: The K-h relationship revisited. *In* Spencer J. E. and Titley S. R. (eds.) Ores and Orogenesis; *Circum-Pacific Tectonics, Geologic Evolution, and Ore Deposits*, pp. 187–202, Arizona Geological Society, Digest 22, Tuscon, AZ.
KLEIN E. M. & LANGMUIR C. H. 1987. Global correlations of ocean ridge basalt chemistry with axial depth and crustal thickness. *Journal of Geophysical Research* **92**, 8089–115.
LALLEMAND S. 2001. *La subduction océanique*. Gordon and Breach Science Publishers, Amsterdam.
LE BAS M. J. 2000. IUGS reclassification of the high-mg and picritic volcanic rocks. *Journal of Petrology* **41**, 1467–70.
LEE C.-T. A., LUFFI P., PLANK T., DALTON H. & LEEMAN W. P. 2009. Constraints on the depths and temperatures of basaltic magma generation on Earth and other terrestrial planets using new thermobarometers for mafic magmas. *Earth and Planetary Science Letters* **279**, 20–33.
MARTINEZ F., FRYER P. & BECKER N. 2000. Geophysical characteristics of the southern Mariana Trough, 11°50′N-13°40′N. *Journal of Geophysical Research* **105** (16), 591–16.
MARTINEZ F. & STERN R. J. 2009. The Southern Mariana Convergent Margin: A Pre-Ophiolite Analogue. *American Geophysical Union, Fall Meeting 2009*, abstract#T33D-05, San Fransisco.
MICHIBAYASHI K., OHARA Y., STERN R. J. *et al.* 2009. Peridotites from a ductile shear zone within backarc lithospheric mantle, southern Mariana Trench: Results of a Shinkai 6500 dive. *Geochemistry Geophysics Geosystems* **10**, Q05X06. doi: 10.1029/2008GC002197
MILLER M. S., GORBATOV A. & KENNETT B. L. N. 2006a. Three-dimensional visualization of a near-vertical slab tear beneath the southern Mariana arc. *Geochemistry Geophysics Geosystems* **7**, Q06012. doi:10.1029/2005gc001110
MILLER M. S., KENNETT B. L. N. & TOY V. G. 2006b. Spatial and temporal evolution of the subducting Pacific plate structure along the western Pacific margin. *Journal of Geophysical Research* **111**, B02401. doi: 10.1029/2005jb003705
MIYASHIRO A. 1974. Volcanic rock series in island arcs and active continental margins. *American Journal of Science* **274**, 321–55.
MOTTL M. J., WHEAT C. G., FRYER P., GHARIB J. & MARTIN J. B. 2004. Chemistry of springs across the Mariana forearc shows progressive devolatilization of the subducting plate. *Geochimica et Cosmochimica Acta* **68**, 4915–33.
OHARA Y. & ISHII T. 1998. Peridotites from the southern Mariana forearc: Heterogeneous fluid supply in mantle wedge. *Island Arc* **7**, 541–58.
OHARA Y., REAGAN M., ISHII T. *et al.* 2008. R/V Yokosuka YK08-08 LEG 2 Cruise Report: Structure and Origin of the Mariana Forearc and Implications for the Origin of the Continental Crust : A Shinkai 6500 Study of the Southern Mariana Forearc. JAMSTEC, Yokosuka.
OHARA Y., REAGAN M., MICHIBAYASHI K. *et al.* 2010. R/V Yokosuka YK10-12 Cruise Report: Composition, Tectonic and Structure of the Mariana Forearc. JAMSTEC, Yokosuka.
OHARA Y., STERN R. J., ISHII T., YURIMOTO H. & YAMAZAKI T. 2002. Peridotites from the Mariana Trough: First look at the mantle beneath an active back-arc basin. *Contributions to Mineralogy and Petrology* **143**, 1–18.
PARKINSON I. J. & PEARCE J. A. 1998. Peridotites from the Izu–Bonin–Mariana Forearc (ODP Leg 125): Evidence for Mantle Melting and Melt–Mantle Interaction in a Supra-Subduction Zone Setting. *Journal of Petrology* **39**, 1577–618.
PEARCE J. A., STERN R. J., BLOOMER S. H. & FRYER P. 2005. Geochemical mapping of the Mariana arc-basin system : Implications for the nature and distribution of subduction components. *Geochemistry Geophysics Geosystems* **6**, Q07006. doi:10.1029/2004GC000895
PECCERILLO A. & TAYLOR S. R. 1976. Geochemistry of Eocene calcalkaline volcanic rocks from the Kastamonu Area, Northern Turkey. *Contributions to Mineralogy and Petrology* **58**, 63–81.
REAGAN M. K., ISHIZUKA O., STERN R. J. *et al.* 2010. Fore-arc basalts and subduction initiation in the Izu–Bonin–Mariana system. *Geochemistry Geophysics Geosystems* **11**, Q03X12. doi: 10.1029/2009GC002871
ROEDER P. L. & EMSLIE R. F. 1970. Olivine-liquid equilibrium. *Contributions to Mineralogy and Petrology* **29**, 275–89.
SATO H. & ISHII T. 2011. Petrology and mineralogy of mantle peridotites from the Southern Marianas. *In* Ogawa Y., Anma R. and Dilek Y. (eds.) *Accretionary Prisms and Convergent Margin Tectonics in the Northwest Pacific Basin, Modern Approaches in Solid Earth Sciences*, pp. 129–47, Springer, 8, Houten, The Netherlands.

Savov I. P., Ryan J. G., D'antonio M. & Fryer P. 2007. Shallow slab fluid release across and along the Mariana arc-basin system: Insights from geochemistry of serpentinized peridotites from the Mariana fore arc. *Journal of Geophysical Research* **112**, B09205. doi: 10.1029/2006JB004749

Savov I. P., Ryan J. G., D'antonio M., Kelley K. & Mattie P. 2005. Geochemistry of serpentinized peridotites from the Mariana Forearc Conical Seamount, ODP Leg 125: Implications for the elemental recycling at subduction zones. *Geochemistry Geophysics Geosystems* **6**, Q04J15. doi: 10.1029/2004GC000777

Schellart W. P., Freeman J., Stegman D. R., Moresi L. & May D. 2007. Evolution and diversity of subduction zones controlled by slab width. *Nature* **446**, 308–11.

Shaw A. M., Hauri E. H., Fischer T. P., Hilton D. R. & Kelley K. A. 2008. Hydrogen isotopes in Mariana arc melt inclusions: Implications for subduction dehydration and the deep-Earth water cycle. *Earth and Planetary Science Letters* **275**, 138–45.

Shen Y. & Forsyth D. W. 1995. Geochemical constraints on initial and final depths of melting beneath mid-ocean ridges. *Journal of Geophysical Research* **100**, 2211–37.

Smith W. H. F. & Wessel P. 1990. Gridding with continuous curvature splines in tension. *Geophysics* **55**, 293–305.

Stern R. J. 2002. Subduction Zones. *Reviews of Geophysics* **40**, 37. doi:10.1029/2001RG000108

Stern R. J. 2010. The anatomy and ontogeny of modern intra-oceanic arc systems. *In* Kusky T. M., Zhai M.-G. and Xiao W. (eds.) *The Evolving Continents: Understanding Processes of Continental Growth*, pp. 7–34, Geological Society of London, Special Publication 338, London.

Stern R. J. & Bloomer S. H. 1992. Subduction zone infancy: Examples from the Eocene Izu–Bonin–Mariana and Jurassic California arcs. *Geological Society of America Bulletin* **104**, 1621–36.

Stern R. J., Fouch M. & Klemperer S. L. 2003. An overview of the Izu–Bonin–Mariana subduction factory. *In* Eiler J. and Hirschmann M. (eds.) *Inside the Subduction Factory*, pp. 175–222, AmericanGeophysical Union, Geophysical Monograph 138, Washington, DC.

Stern R. J., Kohut E., Bloomer S. H., Leybourne M., Fouch M. & Vervoort J. 2006. Subduction factory processes beneath the Guguan cross-chain, Mariana Arc: No role for sediments, are serpentinites important? *Contributions to Mineralogy and Petrology* **151**, 202–21.

Stern R. J., Tamura Y., Masuda H. *et al*. 2013. How the Mariana Volcanic Arc ends in the south. *Island Arc* **22**, 133–48.

Taylor B. & Martinez F. 2003. Back-arc basin basalt systematics. *Earth and Planetary Science Letters* **210**, 481–97.

Tibi R., Wiens D. A. & Yuan X. 2008. Seismic evidence for widespread serpentinized forearc mantle along the Mariana convergence margin. *Geophysical Research Letters* **35**, L13303. doi: 10.1029/2008gl034163

Van Keken P. E., Kiefer B. & Peacock S. M. 2002. High-resolution models of subduction zones: Implications for mineral dehydration reactions and the transport of water into the deep mantle. *Geochemistry Geophysics Geosystems* **3**, 1056. doi:10.1029/2001GC000256

Wada I., Rychert C. A. & Wang K. 2011. Sharp thermal transition in the forearc mantle wedge as a consequence of nonlinear mantle wedge flow. *Geophysical Research Letters* **38**, L13308. doi: 10.1029/2011gl047705

Wade J. A., Plank T., Stern R. J. *et al*. 2005. The may 2003 eruption of Anatahan volcano, Mariana Islands: Geochemical evolution of a silicic island-arc volcano. *Journal of Volcanology and Geothermal Research* **146**, 139–70.

Wallace L. M., Mc Caffrey R., Beavan J. & Ellis S. 2005. Rapid microplate rotations and backarc rifting at the transition between collision and subduction. *Geology* **33**, 857–60.

Wessel P. & Smith W. H. F. 1995a. New version of the Generic Mapping Tools released. *EOS Transactions American Geophysical Union* 76, 329, AGU, Washington, D.C.

Wessel P. & Smith W. H. F. 1995b. New version of the Generic Mapping Tools released. *EOS Transactions American Geophysical Union* electromic supplement [online]. [Cited 17 July 2012]. Available from http://www.agu.org/eos_elec/951546.html, AGU, Washington, D.C.

Wessel P. & Smith W. H. F. 1998. New, improved version of Generic Mapping Tools released. *EOS Transactions American Geophysical Union* 79, 579, AGU, Washington, D.C.

Wheat C. G., Fryer P., Fisher A. T. *et al*. 2008. Borehole observations of fluid flow from South Chamorro Seamount, an active serpentinite mud volcano in the Mariana forearc. *Earth and Planetary Science Letters* **267**, 401–9.

SUPPORTING INFORMATION

Additional Supporting Information may be found in the online version of this article at the publisher's web-site:

Supporting Information S1: Description of the dives.
Fig. S1.1 Cross sections of SEMFR rifts 1, 2 and 3 from the trench.
Fig. S1.2 Dive tracks of Shinkai dives 1096, 1230 and 1235 and deep-tow camera 82.

Fig. S1.3 Dive tracks of YKDT 85, 86, 87 and 88.
Fig. S1.4 Dive tracks of Shinkai dive 973 from YK06-12 cruise report and Kaiko dive 163 from KR00-03 Leg 2 cruise report.
Fig. S1.5 Interpreted bathymetric profile of the eastern flank of rift 1 traversed during Shinkai dive 1096.
Fig. S1.6 Interpreted bathymetric profile of the eastern flank of rift 2 traversed during Shinkai dive 1230.
Fig. S1.7 Interpreted bathymetric profile of the eastern flank of rift 3 traversed during Shinkai dive 1235.
Fig. S1.8 Interpreted bathymetric profile of the eastern flank of rift 1 traversed during Shinkai dive 973.
Fig. S1.9 Interpreted bathymetric profile of the summit of ridge on the eastern side of rift 3 traversed during YKDT-85.
Fig. S1.10 Interpreted bathymetric profile of the eastern flank of ridge of rift 3 (central part of SEMFR) traversed during YKDT-86.
Fig. S1.11 Interpreted bathymetric profile of YKDT-82, performed on the summit of a ridge between rifts 2 and 3
Fig. S1.12 Interpreted bathymetric profile of the axial valley of rift 3 traversed during YKDT-87.
Fig. S1.13 Interpreted bathymetric profile of the eastern flank of ridge of rift 2 performed during YKDT-88.
Fig. S1.14 Interpreted bathymetric profile of Toto caldera performed during Kaiko dive 163.
Fig. S1.15 Interpreted bathymetric profile along the Malaguana–Gadao Ridge (MGR) performed during Kaiko dive 164, near the 13°N magmatic chamber.
Table S1.1 Longitude and latitude of the dives in the SEMFR, MGR and Toto caldera with their depth and trench distance.
Table S1.2 Variation of the width and depth (km) of the three SEMFR rifts along axis.
Supporting Information S2 Sample selection and analytical techniques.
Fig. S2.1 Location of the analyzed samples, for major elements during this study, on the bathymetric profiles of the Shinkai dives 1096, 1230 and 1235.
Supporting Information S3 Method for describing the samples.
Supporting Information S4 Petrographic description and mineralogy of the samples.
Fig. S4.1 SEMFR mineral compositions in clinopyroxene, plagioclase and olivine.
Table S4.1 Representative mean clinopyroxene composition.
Table S4.2 Representative mean plagioclase composition.
Table S4.3 Representative mean olivine composition.
Table S4.4 Representative mean spinel composition.
Supporting Information S5 Correlation between mineral abundances and whole rock chemistry.
Fig. S5.1 Plot showing the correlation between mineral abundances and whole rock composition. A) The olivine proportions are positively correlated to the whole rock Mg#.
Supporting Information S6 Effects of the variations of the Fo content on the P–T conditions of SEMFR mantle melting.